From Morphology to Computation: How Synaptic Organization Shapes Place Fields in CA1 Pyramidal Neurons

Simone Tasciotti[1,2], Daniel Maxim Iascone[3], Spyridon Chavlis[2], Luke Hammond[3,#], Yardena Katz[3], Attila Losonczy[3,4], Franck Polleux[3,4], Panayiota Poirazi[2,5]

[1] Department of Biology, University of Crete, Heraklion, Greece

[2] Institute of Molecular Biology and Biotechnology, Foundation for Research and Technology Hellas, Heraklion, Greece

[3] Mortimer B. Zuckerman Mind Brain Behavior Institute, Columbia University, New York, NY, USA

[4] Department of Neuroscience, Columbia University, New York, NY, USA

[5] Lead contact

[#] Present address: Department of Neurology, The Ohio State University, Wexner Medical School, Columbus, Ohio, USA

* Corresponding author

Abstract

The synaptic mechanisms driving feature selectivity in specific neuron types remains a fundamental and unresolved challenge in neuroscience. In hippocampal CA1 pyramidal neurons (PNs), the development of place selectivity, manifested as place fields, is believed to result from dendritic integration of spatially distributed inputs combined with behavioral time scale plasticity (BTSP). BTSP involves dendritic spikes that temporally regulate synaptic potentiation and depotentiation. However, the role of excitatory (E) and inhibitory (I) synaptic distributions in the emergence of place specificity in CA1 PNs remains unclear, due to the lack of detailed synaptic reconstructions in vivo. Here, we present full synaptic reconstructions from individual CA1 PNs in the mouse hippocampus, revealing that these neurons receive approximately 10,000–15,000 E synapses and 900–1,400 I synapses. Computational modeling of biologically relevant E and I synaptic distributions shows that spatial tuning is preserved with co-tuned, spatially clustered E synapses, but disrupted when E distributions are randomized. Moreover, synapse clustering has a different contribution to spatial tuning in apical vs. basal domains. Our results reveal a complex and finely-tuned interplay between presynaptic input patterns and the spatial organization of their postsynaptic targets in dictating neuronal output in CA1 PNs.

Keywords

dendritic computation, synaptic clustering, CA1, pyramidal neuron, biophysical model, morphology, dendritic nonlinearity, dendritic domains

Introduction

The hippocampus and particularly its CA1 region plays a crucial role in spatial navigation. CA1 pyramidal neurons (PNs), specifically the spatially tuned ‘place cells’, are widely hypothesized

to construct cognitive maps of the environment by combining spatial information and contextual cues[1–3]. Studies have shown that place cells are highly dynamic, undergoing remapping when an animal encounters a new or altered environment[2,4]. During remapping, CA1 place cells reorganize their spatial firing patterns in response to environmental changes, effectively encoding a new cognitive map[5]. In familiar settings, place cells exhibit stable firing fields, supporting the retrieval of established memories, while in novel contexts, rapid remapping enables the encoding of new spatial information.

This flexibility stems from the integrative properties of CA1 PNs, which allow them to adjust the salience of specific input streams based on the environmental context[6,7]. However, the electrophysiological and structural variability of these neurons hinders our in-depth understanding of their computational capabilities[8]. Numerous studies have attempted to characterize how these properties, along with the organization of synaptic inputs, collectively shape the input-output dynamics of CA1 PNs[8–14]. Yet, the impact of the spatial distribution of E and I synaptic inputs on the formation and functional features of place cells remain largely unexplored. Synaptic organization along the dendritic arbor heavily influences the integrative properties of neurons. For example, projections from the CA3 region predominantly target proximal perisomatic dendrites, while long-range inputs from the entorhinal cortex (EC) innervate the distal apical dendrites[15,16]. This anatomical segregation allows both the independent processing of distinct information streams and their conditional integration, thus dynamically shaping the neuron's feature selectivity[17–19]. Additionally, differential ion channel distributions and morphological features of dendrites across these CA1 layers modulate synaptic efficacy, such that identical inputs can have variable impacts on neuronal output depending on their dendritic location[20,21]. A comprehensive exploration of how different E and I incoming inputs shape the local dendritic properties is essential for elucidating the mechanisms underlying neuronal information processing.

Previous results suggested that rat CA1 PNs are characterized by non-uniform synaptic distributions at the sub-branch level[9]. This type of synaptic arrangement can greatly affect the

70 dendritic input-output function[22,23]. For example, synchronous activation of synapses within
71 the same branch was shown to drive strong nonlinear dendritic responses[24–26], a property that
72 generalizes to other cell types[27–29]. These nonlinear dendritic responses were eliminated when
73 the same synapses were distributed across different dendrites[24,26], highlighting the importance
74 of synaptic distribution on CA1 input-output mapping.

75 The abovementioned effects are underlined by voltage-dependent ionic conductances in
76 dendrites, which enable the induction of local regenerative events, turning the neuron into a
77 complex processing system with enhanced computational capabilities[22,24,26,30–32]. As the
78 spatio-temporal organization of synaptic inputs is essential for triggering these local events,
79 synapse location truly matters[24,26,32]. Localized within dendritic compartments that host
80 numerous nonlinear mechanisms, synapses engage in dynamic interactions, amplifying,
81 attenuating, or gating signals based on their dendritic positions, which suggests that the
82 formation and maintenance of synaptic contacts is not a randomized process but an actively
83 regulated mechanism[33–38]. Recent findings further reveal that co-tuned inputs frequently
84 converge onto spatially clustered synapses, creating dendritic “hotspots” that can more easily
85 produce non-linear dendritic events[39,40], as suggested by earlier theoretical work[26,32,41].
86 Therefore, it is clear that to fully understand how CA1 PNs compute a place field, it is essential
87 to consider the spatiotemporal organization of their incoming inputs.

88 In this study, we combined experimental and computational modelling approaches to map the
89 spatial distribution of all E and I synapses in a subset of mouse CA1 PNs in order to investigate
90 how the spatial distribution of E and I synapses affects the output of spatially tuned CA1 PNs.
91 We first employed an advanced sparse labeling technique to reconstruct the complete
92 morphologies of CA1 PNs with high precision. We meticulously traced the dendritic
93 arborizations and mapped the locations and morphological features of both inhibitory and
94 excitatory synapses. We found a non-uniform distribution of excitatory synapses across the
95 dendritic arbor, in contrast to a more homogeneous arrangement of inhibitory synapses.
96 Specifically, terminal dendrites in both apical and basal dendritic domains had higher spine

density than intermediate ones, which resulted in a higher probability of finding large spines located in close proximity (i.e., spine clustering) within terminal dendritic compartments. These data were used to build biophysical models that were extensively validated against electrophysiological data and used to investigate how the spatial distribution of synaptic inputs influences the output of place cells during simulated exploration of a linear track. Models predicted that the spatial allocation of excitatory inputs strongly influences both the spatial tuning and the place cell properties of simulated neurons. Specifically, spatial tuning that was present in simulations using co-tuned and spatially clustered excitatory synapses but was disrupted when target locations were randomized. Moreover, our models suggest that there might be a set of optimal, domain-specific input patterns that impinge on the reconstructed synapses and turn these neurons into high quality place cells. Specifically, we predict that inputs to the distal apical tuft are more effective when activated in large clusters whereas inputs to the basal dendrites are more effective when synaptic clusters are distributed over multiple branches. Together, our findings reveal a complex and finely-tuned interplay between presynaptic input patterns and the spatial organization of their postsynaptic targets in specifying the output properties of CA1 PNs.

Results

Reconstruction of CA1 Pyramidal Neuron Morphology

To reconstruct the dendritic morphology and synaptic distribution of all excitatory and inhibitory synapses of mouse dorsal CA1 PNs at single-cell resolution *in vivo*, we deployed a combination of sparse reporter expression, imaging, and computational tracing methods that we previously developed[42]. We labeled dorsal CA1 PNs through *in utero* electroporation of plasmids expressing Cre-dependent Flex-tdTomato (red cell filler) Flex-EGFP-Gephyrin (inhibitory synaptic marker) along with low levels of a Cre recombinase plasmid for targeted,

122 sparse labeling[43,44] (**Figure 1A**). After high-resolution confocal imaging (**Figure 1B**), we used
123 open-source reconstruction software Vaa3D[45] to obtain a trace of the dendritic tree (**Figure**
124 **1C**). Through the Vaa3D Synapse Detector toolkit[42], we annotated all excitatory and inhibitory
125 synapses located within each segment of the dendritic tree. Given that the majority of
126 excitatory synapses in CA1 PNs occur on spines[9], we used them as a structural proxy of all
127 excitatory synapses in our neurons. Inhibitory synapses were identified by co-localizing EGFP-
128 Gephyrin puncta with cytosolic tdTomato (**Figure 1B**). Using this method, we obtained detailed
129 information about each synapse's position and shape, including features like volume, spine
130 head diameter, and spine neck length. We also identified the relative location of inhibitory
131 synapses, whether on the dendritic shaft or a dually innervated spine. Finally, Vaa3D
132 algorithms linked all synaptic features to the corresponding branch segment node, and neuron
133 trace fragments of the same neuron from serial tissue sections were stitched together to create
134 complete morphological reconstructions. Through this method, we obtained the dendritic arbor
135 morphology and excitatory (**Figure 1D**) and inhibitory (**Figure 1E**) synapse mapping of six
136 CA1 PNs (with one that lacks the inhibitory synapse map). After implementing the synaptic
137 reconstruction pipeline, we applied a custom smoothing algorithm to dendritic diameter
138 measurements to eliminate minor artifacts introduced by the reconstruction software (**see**
139 **Methods, Figure S1**). From the structural analysis of these neurons, we observed, on
140 average, 11,796±2,212 (mean±std, n=6 neurons, std: standard deviation) spines and 741±
141 545 inhibitory synapses, distributed over 7,164±982 μm of average total dendritic length.
142 Consistent with previous studies[46], the average spine density was estimated to be 1.41±0.18
143 while the inhibitory synapse density was 0.10±0.07[47] (**Figure 1F**).

144

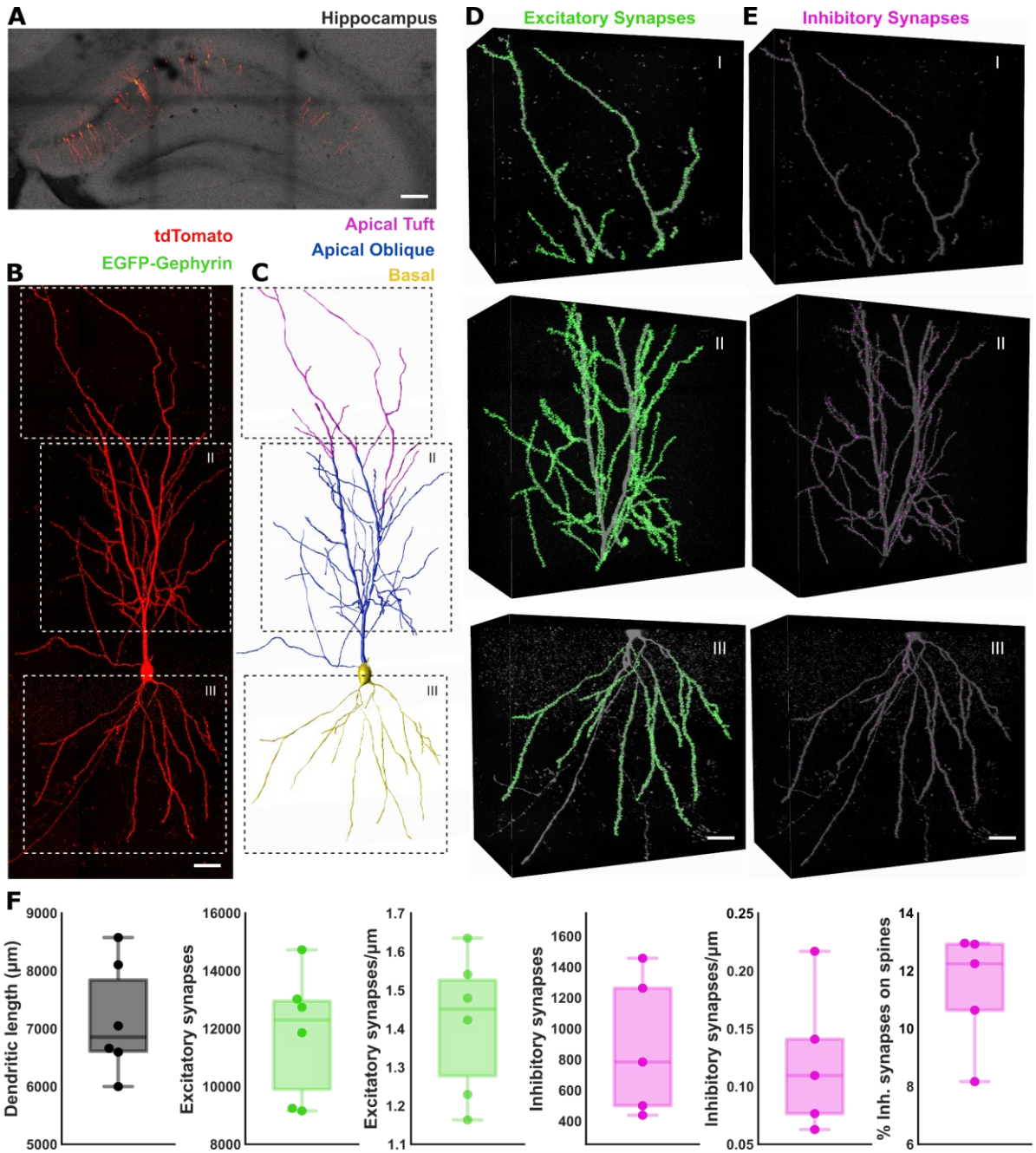

(For high quality version, refer to the end of the document)

Figure 1: Reconstruction and analysis of all excitatory and inhibitory synapses across CA1 pyramidal neurons. A. Sparsely labeled pyramidal neurons expressing tdTomato (red) and EGFP-Gephyrin (green) in hippocampal CA1. Grey: tissue autofluorescence using 488nm excitation. Scale bar: 300 µm. **B**. Single-synapse resolution image of a CA1 pyramidal neuron expressing tdTomato (red) and EGFP-Gephyrin (green). Scale bar: 60 µm. **C**. Dendritic arbor of whole CA1 PN shown in panel B, annotated to highlight apical tuft dendrites (magenta), apical oblique and apical trunk dendrites (blue) and basal dendrites (yellow). **D-E**. All dendritic spines (excitatory synapses; D, green) and Gephyrin+ inhibitory synapses (E, purple) annotated throughout the dendritic arbor (grey)

154 of the example CA1 PN reconstructed within insets from (B-C). Scale bars: 50 µm. **F.** Quantitative analysis of all
155 CA1 PNs reconstructed showing dendritic structure and synaptic distribution. From left to right: total dendritic length
156 distributions (µm); total number of excitatory synapses and their density (syn/µm); total number of inhibitory
157 synapses and their density (syn/µm); percentage of inhibitory synapses localized on a spine (dually innervated
158 spines).

159 **Domain-Specific Analysis of Synaptic Organization in CA1 PNs**

160 CA1 PNs exhibit significant variability in the structural and electrophysiological properties of
161 their dendritic arbors, which are also targeted by different presynaptic sources[8,9,48,49].
162 Consequently, we opted to analyze the synaptic organization by subdividing the dendrites into
163 four distinct domains, namely *Basal*, *Apical Trunk*, *Oblique*, and *Tuft* dendritic domains. Within
164 each domain, we further distinguished intermediate and terminal branches based on their
165 relative branch order, referred to as *subdomains* (**Figure 2A**). We found that peri-somatic and
166 intermediate dendritic regions exhibit a substantially lower spine density than more terminal
167 branches (**Figure 2B**), which is in line with the literature[9,46] while inhibitory synapses show no
168 significant variation across subdomains (**Figure 2B**).

169 Within these dendritic subdomains, we also characterized the size of synaptic connections in
170 order to infer the degree of potentiation as a function of the dendritic subdomain. Synaptic
171 volume corresponds to spine head size or postsynaptic density size for excitatory and
172 inhibitory synapses, respectively, and is linearly correlated with synaptic strength[22,50,51]. As
173 described in **Iascone et al.** (**2020**)[42] for layer 2/3 PNs in the mouse primary somatosensory
174 cortex, we used the Synapse Detector tool to map the distribution of synaptic strengths across
175 all different subdomains. Large synapses were defined as those exceeding the 80th percentile
176 of the synaptic volume distribution of each cell. We found similar distributions of large
177 synapses across dendritic subdomains, with the exception of the terminal Tuft, which exhibited
178 a greater percentage of large spines compared to its intermediate counterpart (**Figure 2C**).

179 Another structural characteristic that may indicate an important function is the increase of
180 synaptic density in a branch-specific way. During learning, new spines tend to form in proximity

181 to already existing spines, or appear in small clusters, and to be more stable, marking
182 clustered potentiation at branch level[38,52–56]. To check this possibility, we compared the
183 experimentally observed variation (standard deviation, in short STD) in E and I synapse
184 density within dendritic subdomains to the synaptic densities of a subdomain-wise null
185 distribution (**see Methods**) for each neuron. Dendritic subdomains with STD higher than that
186 of the null distribution exhibit this branch-specific enrichment. We found branch-specific
187 enrichment of excitatory synapses in the Trunk and Intermediate Basal domains, whereas
188 inhibitory synapses were overall uniformly distributed (**Figure 2D**).

189

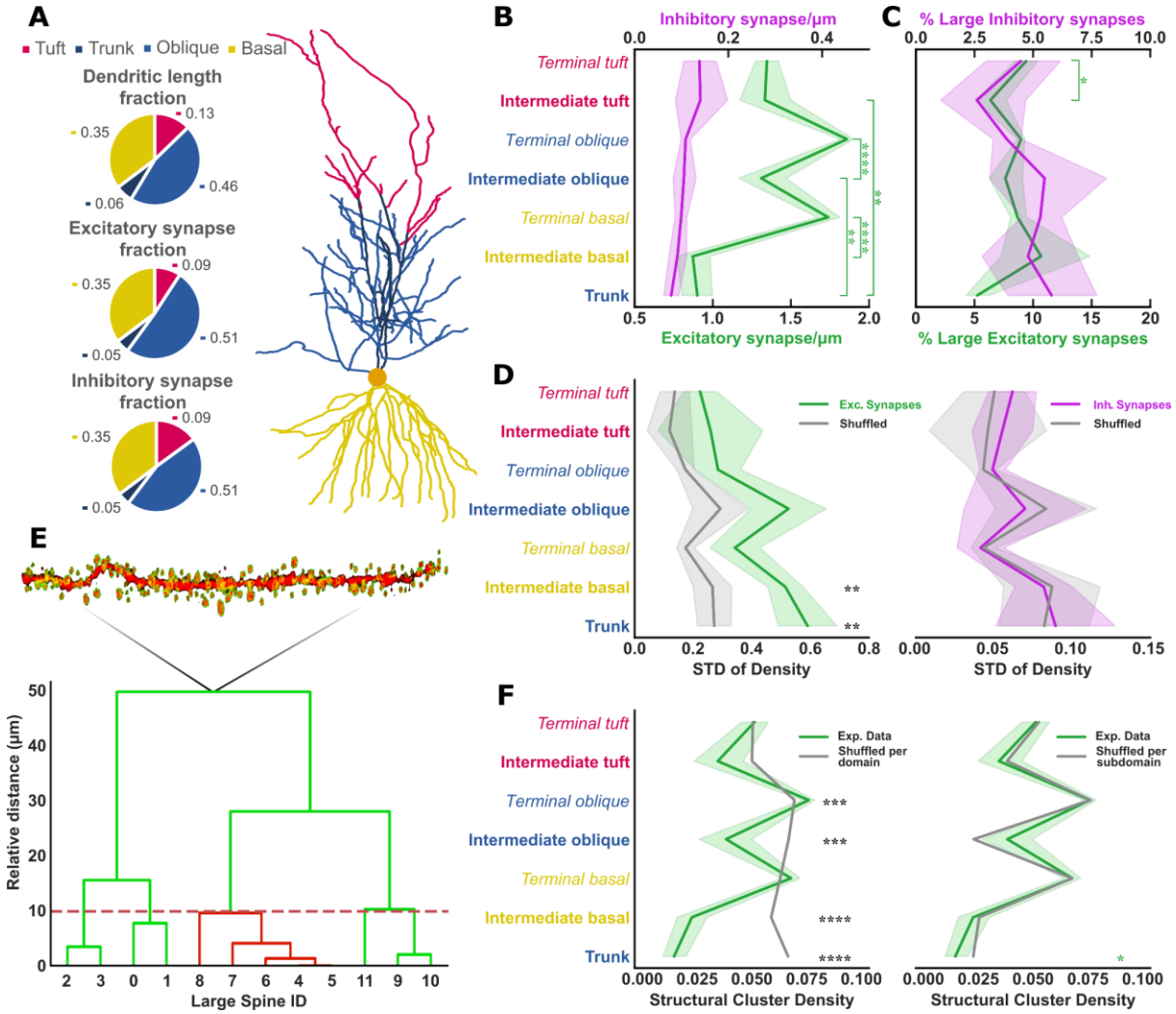

190

191 **Figure 2: Analysis of Dendritic Subdomains and Synaptic Distributions. A.** Left: pie charts showing the
192 percentage of excitatory (E) and inhibitory (I) synapses located in different domains. Right: schematic

representation of a CA1 PN, with distinct dendritic domains highlighted in different colors. These include the Basal (green), Tuft (pink), Trunk, and Oblique (blue), further subdivided into intermediate and terminal subdomains using darker and lighter colors, respectively. **B.** Density of E and I synapses across different subdomains. **C.** Percentage of large spines (i.e., spines with a volume above the 80th percentile of the size distribution) for each subdomain. **D.** Variation (standard deviation, STD) in E and I synapse densities for each subdomain. Experimentally observed STDs (green/purple) are compared to those expected from a random redistribution of synapses within their specific subdomains (grey). Specifically, synapses were randomly shuffled across branches within the same subdomain, and excitatory/inhibitory synaptic density variation was recalculated. Excitatory -but not inhibitory- synapse variability is significantly different from the shuffled distribution (2-way ANOVA for spines density std: distribution: $F(1, 4228)=374.74$, $p=4.63e-80$; domain: $F(6, 4228)=794.07$, $p=0.00e+00$; distribution x domain: $F(6, 4228)=10.66$, $p=8.71e-12$). **E.** Schematic illustration of the hierarchical clustering algorithm used to identify spine clusters. The algorithm detects groups of large spines (with volumes above the 80th percentile) that are located within 10 micrometers of each other. The dashed line indicates the 10 µm distance cutoff. Red dendrogram strokes represent a spine cluster. **F.** Density of spine clusters across subdomains. Left: experimentally observed distribution (green) vs. a domain-wise shuffled distribution (grey). Right: experimentally observed distribution vs. a branch-wise shuffled distribution. Statistically significant differences are found only between the experimentally observed distribution and the shuffled-per-domain distribution. (2-way ANOVA for cluster density between `Exp. Data` and `Shuffled`: protocol: $F(1, 775761)=136.83$, $p<10^{-30}$; domain: $F(6, 775761) = 3412.82$, $p<10^{-80}$; protocol x domain: $F(6, 775761)=58.33$, $p<10^{-70}$). When shuffling within subdomains, the two distributions substantially overlap, with the exception of the Trunk (2-way ANOVA for cluster density between `Exp. Data` and `Shuffled per subdomain`: protocol: $F(1, 775761)=1.06$, $p=0.303$; domain: $F(6, 775761)=82383.08$, $p<1e^{-6}$; protocol x domain: $F(6, 775761) = 4.58$, $p=1.19e-04$). Pair-wise two-sided t-tests are shown in all plots. $^{*}p < 0.05$, $^{**}p < 0.005$, $^{***}p < 0.001$, and $^{****}p < 0.0001$, corrected for multiple comparisons using Bonferroni's method. Error-bands in **B**, **C**, **D**, and **F** represent 95% confidence interval (CI) of the mean.

Given that excitatory synapses are non-uniformly distributed, we next asked whether there is a finer patterning of synaptic connections within the different subdomains. Over the past decades, several studies demonstrated that the volume of spines tends to increase with the strengthening of the synapse[57–59]. Spines, however, do not grow in isolation but rather interact with neighboring synapses, often resulting in the formation of the so-called synaptic clusters.

223 Indeed, several studies investigated how non-linear dendritic mechanisms promote plasticity
224 of nearby excitatory synapses[24,54,55,60,61]. For this reason, we investigated the presence of
225 structural clusters in the different dendritic subdomains. To do so, we first defined a putative
226 structural cluster as a group of three or more large (as defined previously) synapses within a
227 branch segment of ~10 μm[62]. This approach is based on the assumption that heterosynaptic
228 plasticity drives co-tuned nearby synapses to grow together and deviate from the average
229 size[60,63–66]. We used a hierarchical clustering algorithm for the identification of these putative
230 structural clusters (**Figure 2E**). Our analysis revealed a higher density of structural clusters in
231 the terminal domains, a result that was significantly different from the density distribution
232 obtained through domain-wise shuffling of synapses (**Figure 2F**). However, when comparing
233 these observations with a subdomain-wise null distribution, the differences were no longer
234 significant (**Figure 2F**). This finding suggests that the observed variations in cluster density
235 between domains are primarily driven by differences in synaptic density within the
236 corresponding subdomains.

237 Taken together, our results show that the spatial distribution of excitatory synapses in CA1
238 PNs is not random, showing a clear enrichment for terminal branches in basal and apical
239 oblique dendrites, but not in apical tuft dendrites. However, this fine, domain-specific
240 organization is not found for inhibitory synapses, creating an asymmetric E/I balance.

241

242 From Reconstruction of Synaptic Distribution to Modeling of Neuronal 243 Functional Properties

244 To investigate how E and I synaptic distribution may influence the emergence of spatial tuning
245 in CA1 pyramidal neurons, we constructed a biophysical model for each reconstructed
246 neuronal morphology (**Figure 3A**) and simulated their activity during a virtual linear track
247 exploration task (**Figure 3B**). The models were implemented using the NEURON simulation

environment[67], adhering to the channel distribution parameters established by **Poirazi et al. 2003**[26] **(see Methods**).

Given the high synaptic density in our reconstructed neurons, we employed a fine spatial discretization by increasing the number of segments in the models. This ensured enhanced spatial resolution, enabling us to capture the detailed biophysical interactions between adjacent synapses (**Figure 3C**). To ensure the accuracy and biological relevance of our models, we validated both their passive and active properties against experimentally observed values. Passive properties, including input resistance ($\mathrm{R_{in}}$), membrane time constant (τ_m), Sag Ratio, and dendritic attenuation, were within physiological regimes[8,68,69] (**Figure 3D-4A; see Methods**). Similarly, the active properties, such as somatic and dendritic spiking activity, Frequency-Current (F-I) curve, and dendritic nonlinearities, were validated with widely used protocols[8,24] (**Figure 4B-E; see Methods**).

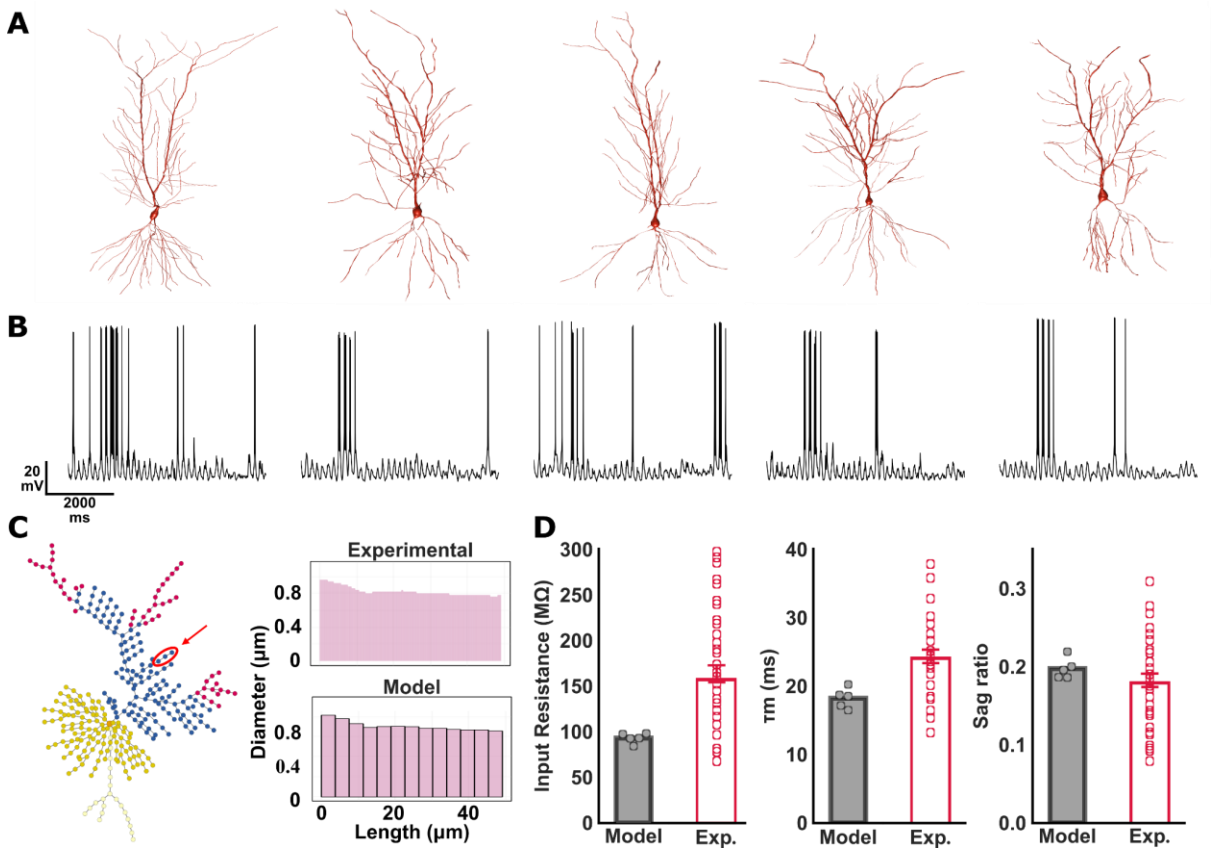

262 **Figure 3: From morphologies to biophysical models. A.** Reconstructions of dendritic morphology of the five
263 CA1 pyramidal neurons used to generate the computational models. **B.** Somatic voltage traces produced by a
264 place-tuned stimulation protocol used on the corresponding neuronal reconstruction. **C.** Left: schematic illustration
265 of the cell's segmentation used in the NEURON simulation environment (obtained using DendroTweaks[70]). Right:
266 example of a branch structure from the data and its corresponding segmentation in the simulator. **D.** Passive
267 membrane properties of CA1 PN models match experimental values. From left to right: input resistance, membrane
268 time constant, and sag ratio. Experimental barplots redrawn from Masurkar et al., 2020[8].

269

270 The excitatory synaptic weights were calibrated based on experimental findings to ensure
271 physiological relevance[71]. Specifically, we implemented the principle of synaptic democracy,
272 which posits that synaptic inputs across the dendritic tree contribute equally to somatic
273 depolarization, regardless of their location[72]. To achieve this, proximal synapses were
274 parameterized to elicit a 0.2 mV depolarization at the soma[20]. For distal synapses, the α-
275 amino-3-hydroxy-5-methyl-4-isoxazolepropionic acid (AMPA) receptor conductance was
276 progressively increased as a function of the distance from the soma[71,73]. This adjustment
277 ensured that while distal synapses generated larger dendritic excitatory postsynaptic
278 potentials (EPSPs), the resulting somatic depolarization remained constant at 0.2 mV (**Figure
279 4F**; **see Methods**). Moreover, considering the large variability of spine sizes observed in our
280 analysis, we decided to account for it in the calculation of the synapse strength by linearly
281 varying the validated weight according to the spine head volume[74] (**see Methods**).

282 Inhibitory synapses were validated differentially based on their presynaptic sources to ensure
283 an accurate representation of their functional characteristics. For this study, inhibitory
284 synapses were assigned to six distinct locomotion active interneuron types, neurogliaform
285 (NGF), oriens-lacunosum moleculare (OLM), parvalbumin-expressing basket (PVbasket),
286 apical dendrite targeting cholecystokinin-expressing (CCK), Bistratified, and Ivy cells, based
287 on their known post-synaptic target distributions across the dendritic tree[75–77]. Synaptic
288 weights, as well as rise and decay times, were calibrated by replicating experimental protocols

289 reported in the literature[78–82] (**Figure 4G**). Similar to their excitatory counterparts, inhibitory
290 synapses were also scaled linearly with the synaptic volume. These rigorous validations
291 enhanced the reliability of the models and ensured they accurately reflected the physiological
292 characteristics of CA1 PNs.

293

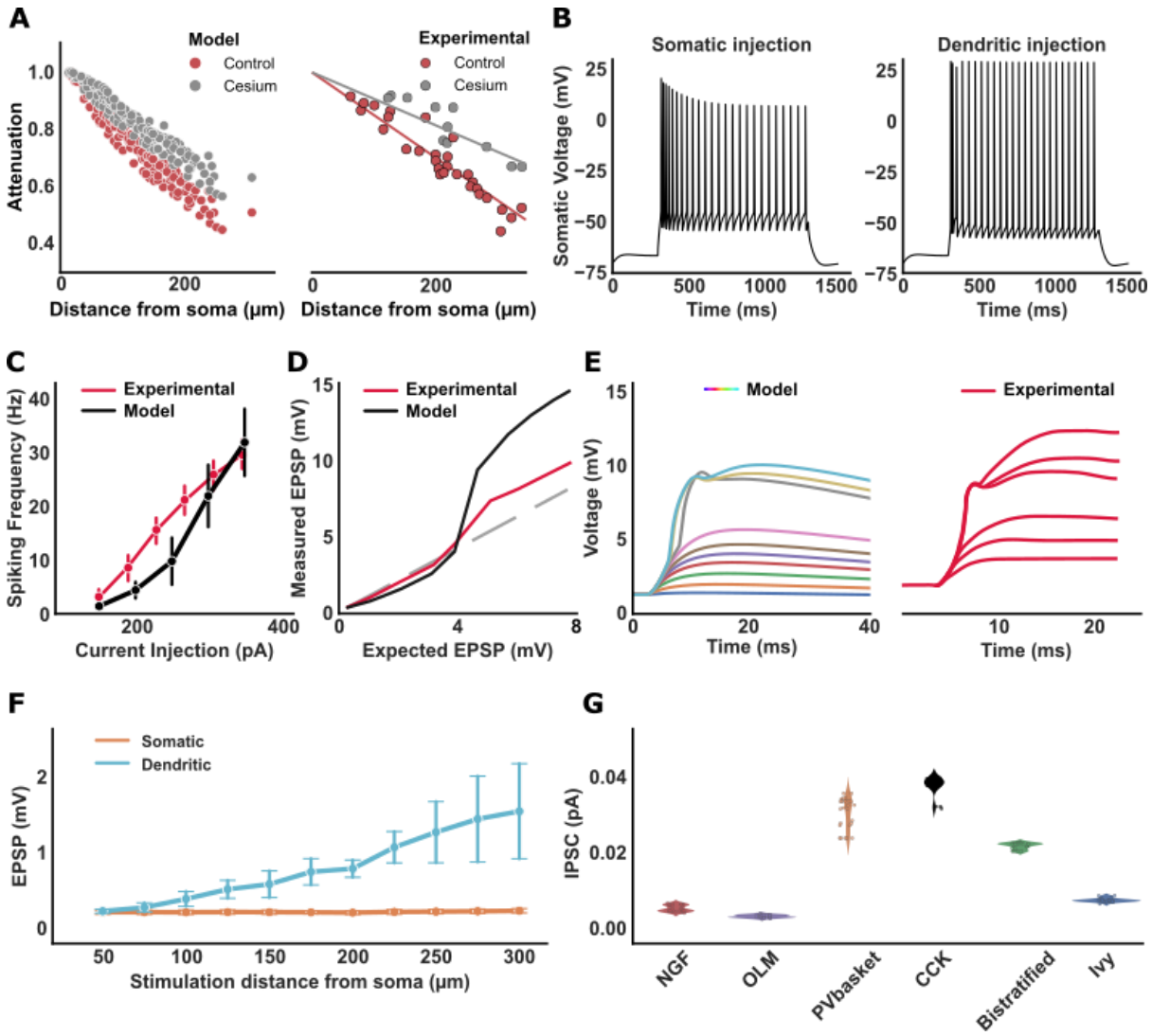

294

295 **Figure 4: Electrophysiological Properties of CA1 PN Models Match Experimental Data. A.** Dendritic
296 attenuation of somatically injected negative current in control conditions (red) or simulating extracellular cesium
297 (grey, 80% reduction of the h-current). Experimental data redrawn from Golding et al., 2005 are similar to model
298 outputs. **B.** Examples of somatic voltage traces induced by a 300 pA current injection in the soma (left) or in a
299 dendrite (right) located at ~250 μm from the soma. **C.** The input-output (Frequency-current (F-I)) curves of the
300 models resemble experimental ones from Masurkar et al., 2020[8]. **D.** Peak amplitude of EPSPs measured at the

301 soma as a function of the expected arithmetic sum of individual EPSPs. Experimental example curve redrawn from
302 Losonczy and Magee, 2006[24]. **E.** Somatic depolarization upon simultaneous excitation of a progressively increasing
303 number of synapses. Left: stimulation of 1 to 30 simulated synapses on an oblique dendrite. Right: spines
304 stimulated through glutamate uncaging, redrawn from Losonczy and Magee, 2006[24]. **F.** Dendritic and somatic
305 excitatory postsynaptic potentials (EPSPs). Synaptic AMPA conductance strength increases with path distance
306 from the soma, ensuring invariant somatic depolarization. **G.** Inhibitory postsynaptic currents (IPSCs) originating
307 from various interneurons, including NGF (neurogliaform cells), OLM (oriens-lacunosum moleculare cells),
308 PVbasket (parvalbumin-expressing basket cells), CCKbasket (cholecystokinin-expressing cells), Bistratified and
309 Ivy cells. Validated to match experimentally observed data. Errorbars in **C**, and **F** represent 95% confidence interval
310 (CI) of the mean.

311

312 After validating the passive and active properties of the individual PNs, we constructed the
313 inputs to reliably reproduce the dynamics of incoming synaptic activity under a linear track
314 exploration task. To achieve this, we produced spike trains that simulate excitatory inputs
315 originating from CA3 and the entorhinal cortex (EC), capturing the neural patterns associated
316 with spatial navigation. Specifically, we modeled convergent EC inputs as multiple grid
317 representations covering a virtual linear track, from which CA3 place-like inputs were derived[6]
318 (**see Methods**). The two resulting input streams were subdivided into a total of 12 place fields,
319 each containing hundreds of co-tuned spike trains. In addition, background synaptic noise was
320 simulated by introducing independent Poisson-distributed, and Gaussian-filtered inputs to
321 CA1 PNs (**Figure 5B**).

322 Inhibitory inputs, conversely, were modeled as theta-filtered, phase-shifted Poisson spike
323 trains, with each presynaptic source tailored to match the specific characteristics reported in
324 the literature[76] (**Figure 5C; see Methods**). All inputs were distributed across synapses located
325 in the anatomically relevant regions of the dendritic tree, ensuring that the simulated activity
326 closely approximated the complex synaptic interactions observed during spatial navigation
327 (**Figure 5A**). In particular, each interneuron targeted a synapse based on a probability derived
328 from a non-linear function that depends on the distance from the soma. (**Figure S2**).

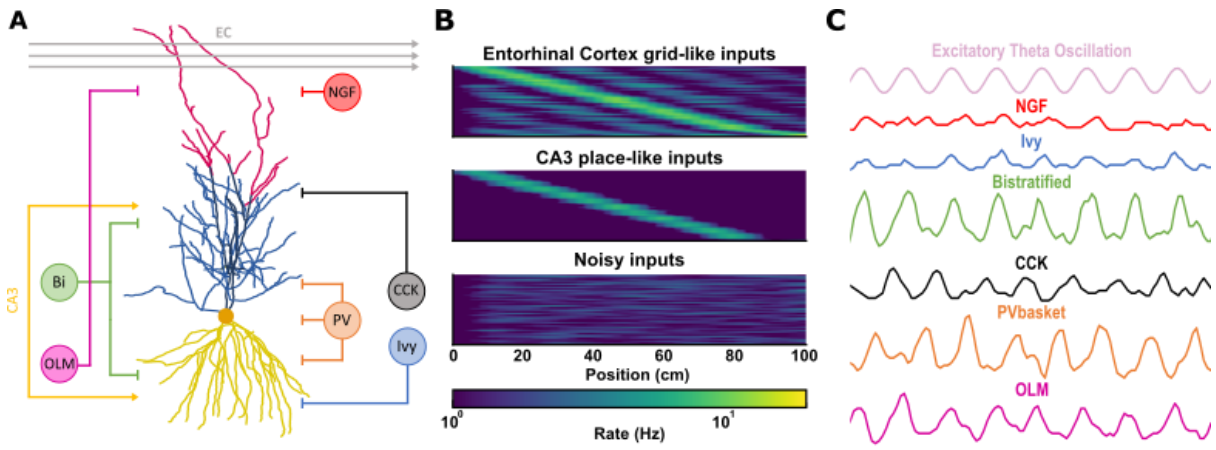

Figure 5: Patterns of Excitatory and Inhibitory Inputs to CA1 Pyramidal Cells. A. Schematic representation of the model neuron depicting excitatory and inhibitory input sources that are organized according to anatomical findings. **B.** Different types of excitatory inputs to the model. From top to bottom: Heatmap of EC grid-like, CA3 place-like and random noise spike trains. Each row represents a different presynaptic input neuron. The colormap is the same across heatmaps and brighter colors denote higher firing rates. **C.** Population activity of simulated interneuron spike trains compared to the Excitatory Theta Oscillation. Firing frequencies and theta phases are based on experimental findings.

Functional Role of Input Clustering in Place Cell Computation

After confirming that our model accurately reproduces the biophysical and electrophysiological properties of CA1 PNs given realistic synaptic input dynamics, we set out to investigate how spatial organization of excitatory synaptic inputs influences place-tuning properties. Specifically, we investigated how the clustering of excitatory synaptic inputs alters the computational capabilities of the neuron in a simulated navigational task.

A recent glutamate imaging study has characterized the spatiotemporal patterns of synaptic inputs to CA1 place cells during navigation on familiar linear tracks[39]. This study revealed that synapses receive inputs across all track locations, but the excitatory drive is significantly higher within the somatic place field than outside it. Additionally, the synapses that are co-

349 tuned with the soma exhibit a greater tendency to form spatial clusters. Given these findings,
350 we generated 1,000 simulated connectivity patterns for each neuronal reconstruction
351 designed to emulate the spatial organization of synaptic inputs that have been observed
352 experimentally. Specifically, each connectivity pattern included a subset of structural clusters,
353 as defined previously, which were preferentially targeted by place-tuned inputs. Inputs
354 associated with a selected place field targeted a higher number of clustered synapses, which
355 determined the somatic place-tuning, while the remaining synapses either received place-
356 tuned or noisy inputs based on a uniform distribution.

357 This allocation protocol resulted in two distinct synaptic populations: (1) co-tuned clustered
358 synapses, referred to as *Functional Clusters*, which were exclusively place-tuned, and (2)
359 dispersed synapses, which were either place-tuned or targeted by noisy inputs. This
360 configuration represented our Clustered condition (**Figure 6A, Control**). To assess the role of
361 synaptic clustering in neuronal computation, we generated alternative synaptic distributions
362 by shuffling the input targets under three different constraints. First, we generated a
363 configuration where the total number of activated synapses was preserved, but inputs were
364 randomly reassigned, disregarding the original preference for clustered synapses, which are
365 larger and stronger (**Figure 6A, Shuffled** – Same Synapse Number (SSN)). Second, since
366 synaptic strength scales with size, we generated a configuration in which the total synaptic
367 volume rather than the number of inputs was preserved. This ensured a closer approximation
368 of the excitatory drive comparable to the Clustered configuration but caused a much larger
369 number of synapses to get activated (**Figure 6A, Shuffled** – Same Synapse Volume (SSV)).
370 Lastly, we generated a configuration where the cumulative synaptic weight was preserved.
371 This configuration considers the volume while also accounting for the "synaptic democracy"
372 adjustment where synaptic conductance scales with the distance from the soma (**Figure 6A,**
373 **Shuffled** – Same Synapse Weight (SSW)). These three shuffled configurations allowed us to
374 disentangle the influence of synaptic clustering, size, and weight in shaping neuronal place
375 computations.

376 To verify that the shuffling protocols disrupted input clustering, we quantified the number of
377 functional synaptic clusters across dendritic domains for each input allocation scheme. As
378 expected, the Clustered configuration exhibited a significantly higher number of functional
379 clusters across all dendritic domains, particularly when compared to the SSN condition, which
380 preserved the number of inputs but disrupted their spatial organization (**Figure 6B**). The SSV
381 protocol, while maintaining a relatively high number of functional clusters due to the increased
382 number of activated synapses, resulted in clusters with a smaller average size and lower total
383 synaptic volume (**Figure S3**). These findings confirm that random shuffling alters the structural
384 properties of synaptic clustering.

385 Next, we evaluated how these different input allocation protocols influenced the simulated
386 activity of CA1 PNs. We found that neurons in the Clustered condition exhibited the
387 characteristic place-field activity, while all shuffling protocols led to its disruption (**Figure 6C**).
388 To quantify the extent of disruption, we assessed specific place field metrics such as in-field
389 and out-field firing frequency, field size and spatial information[83]. We found that only the
390 Clustered configuration generated place-field features, such as In-Field Firing Frequency
391 (**Figure 6D**) and Spatial Information (**Figure 6E**), that aligned qualitatively with experimental
392 results from **Mizuseki et al.** (**2012**)[84]. The SSN configuration resulted in substantially lower
393 firing activity, leading to a marked reduction in Spatial Information. In contrast, both the SSV
394 and SSW configurations led to a much higher firing frequency, with increased spike
395 occurrences outside the place field. This widespread activity diminished the spatial selectivity
396 of neuronal firing, ultimately reducing the overall Spatial Information. These results suggest
397 that synaptic clustering plays a critical role in maintaining the spatial tuning of place cells and
398 perturbing clustering disrupts single-cell encoding of spatial information.

399

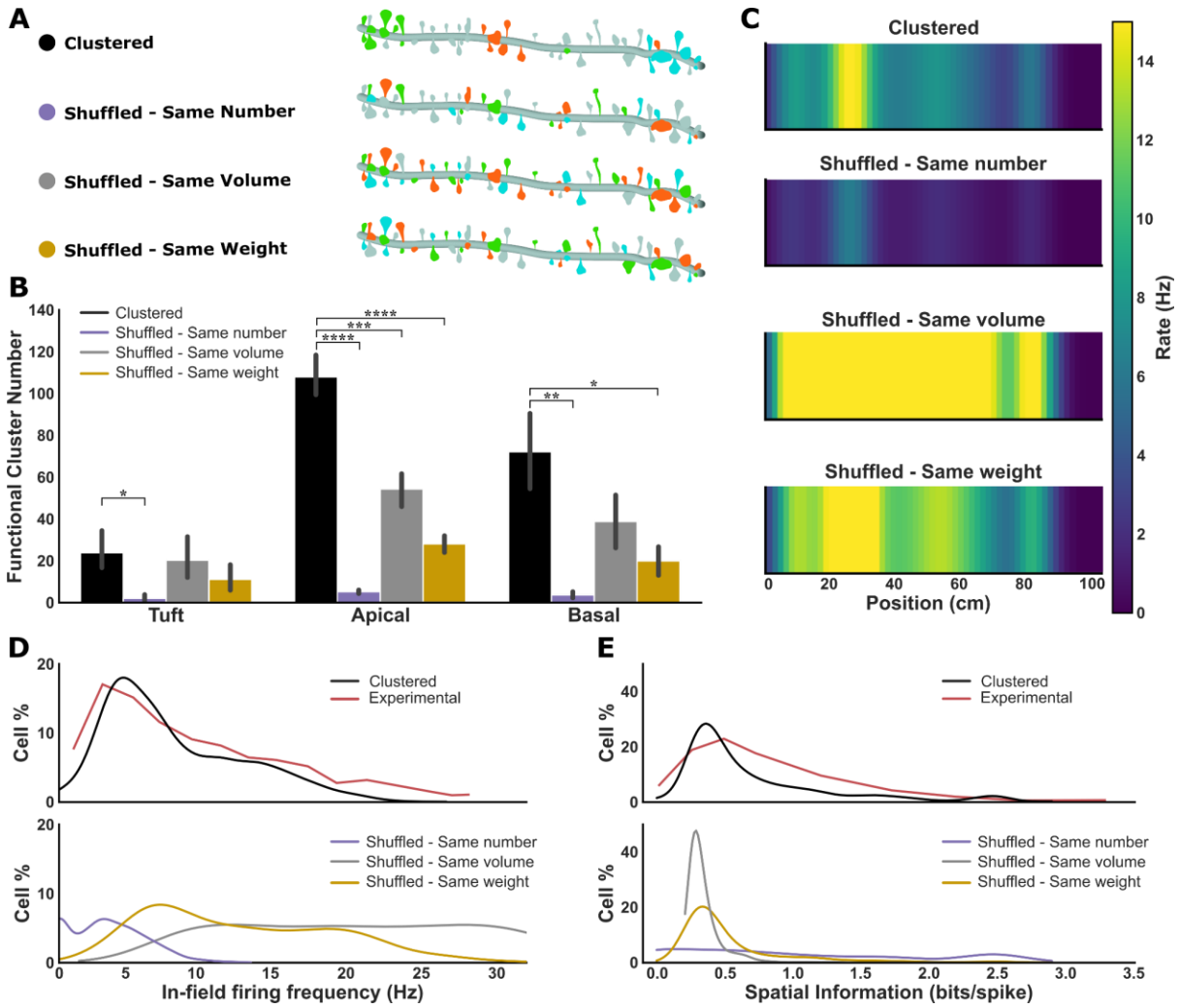

Figure 6: Effect of Synapse Clustering on Spatial Tuning. A. Schematic representation of four different synaptic configurations. Colors represent the tuning of synaptic inputs. Clustered: Synapses within pre-identified structural clusters are more likely to receive co-tuned inputs. Shuffled - Same Number: Inputs are randomly distributed while maintaining the same number of activated synapses as in the Clustered configuration. Shuffled - Same Total Weight: Inputs are randomly distributed while preserving the total synaptic strength of the activated inputs as in the Clustered configuration. Shuffled - Same Total Volume: Inputs are randomly distributed but the total volume of activated synapses remains the same as in the Clustered configuration. **B.** Number of activated functional synaptic clusters (co-tuned synapses located within a 10 µm spatial window) across dendritic domains (Basal, Apical, and Tuft) for each configuration. Statistically significant differences are indicated (2-way ANOVA for the number of Functional Clusters in the Tuft domain: cluster protocol: $F(3, 16)=5.16$, $p=1.10e-02$; Apical domain: cluster protocol: $F(3, 16)=142.96$, $p=9.19e-12$; Basal domain: cluster protocol: $F(3, 16)=19.16$, $p=1.52e-05$). Pair-wise t-test between Control and Shuffled protocols are shown in the plot. $^{*}p < 0.05$, $^{**}p < 0.005$, $^{***}p < 0.001$, and $^{****}p < 0.0001$, corrected for multiple comparisons. Error-bars represent 95% confidence interval (CI) of the mean. **C.** Average activity heatmaps showing place tuning of a population of CA1 PN models stimulated under the different

synaptic configurations. Input shuffling significantly disrupts the output place fields. **D.** Distribution of in-field firing frequencies. Top: The Clustered configuration qualitatively replicates the experimentally observed spatial firing patterns of CA1 PNs as reported by Mizuseki et al. (2012)[84]. Bottom: Firing frequency distributions of the shuffling configurations. **E.** Distribution of spatial information content (measured in bits per spike). Top: The Clustered configuration aligns qualitatively with the experimentally observed spatial firing patterns described by Mizuseki et al. (2012)[84]. Bottom: Spatial information distribution for the shuffling configurations.

Dendritic domain-specific clustering differentially contributes to spatial tuning

While global synaptic clustering alters the place-specific properties of our model CA1 PNs, its role in domain-specific integration remains unclear. To address this question, we probed the contribution of domain-specific clustering features to neuronal output. Specifically, we asked *how* synaptic clusters which are co-tuned with the soma ("in-field" clusters), and are located in the Basal, Apical or Tuft dendrites, contribute to neuronal spatial tuning. We focused on three clustering features: the *Total Cluster Volume* (the cumulative volume of all synapses within in-field-tuned clusters), the *Average Cluster Size* (the mean number of synapses of these clusters), and the *% Dendrites with In-field-Tuned Clusters*, thereby capturing both the strength and spatial distribution of synaptic inputs (**Figure 7A**).

We then applied a machine-learning regression algorithm to evaluate how well these features can predict the spatial tuning properties previously mentioned (**Figure 7B**). While the model accurately predicted in-field and out-field firing rates, suggesting that the structural properties of synaptic clusters strongly influence firing frequency, it poorly predicted field size, indicating that this property may involve more complex mechanisms (**Figure 7C**).

Notably, analysis of feature importance revealed domain-specific strategies for influencing somatic output. In the Tuft domain, *Total Cluster Volume* was the most critical predictor of spatial tuning quality. This suggests that larger clusters or bigger spines may be required to drive local spikes, thus overcoming signal attenuation caused by a large electrotonic distance

441 from the soma (**Figure 7D**) and exert a significant influence on somatic firing[85–87]. In contrast,
442 for the Basal domain, the *% Dendrites with In-field-Tuned Clusters* was the most important
443 predictor of spatial tuning quality. These findings suggest that parallel input streams across
444 multiple branches may represent an optimal strategy for reliably modulating somatic output,
445 highlighting the integration advantages conferred by proximity to the soma (**Figure 7D**). This
446 interpretation is further supported by the application of the SHAP (SHapley Additive
447 exPlanations) framework to explain the output of our Random Forest results[88]. This approach
448 provides a per-feature and per-sample attribution to each individual predictor, highlighting the
449 contribution of each input to the corresponding output value (**Figure S4**).

450 Interestingly, none of the three clustering features could reliably predict somatic output for the
451 Apical domain, a region that in our analysis encompassed both Trunk and Oblique domains.
452 This suggests that the apical compartment may rely on alternative mechanisms to shape
453 spatial tuning that are not captured by the abovementioned clustering features.

454

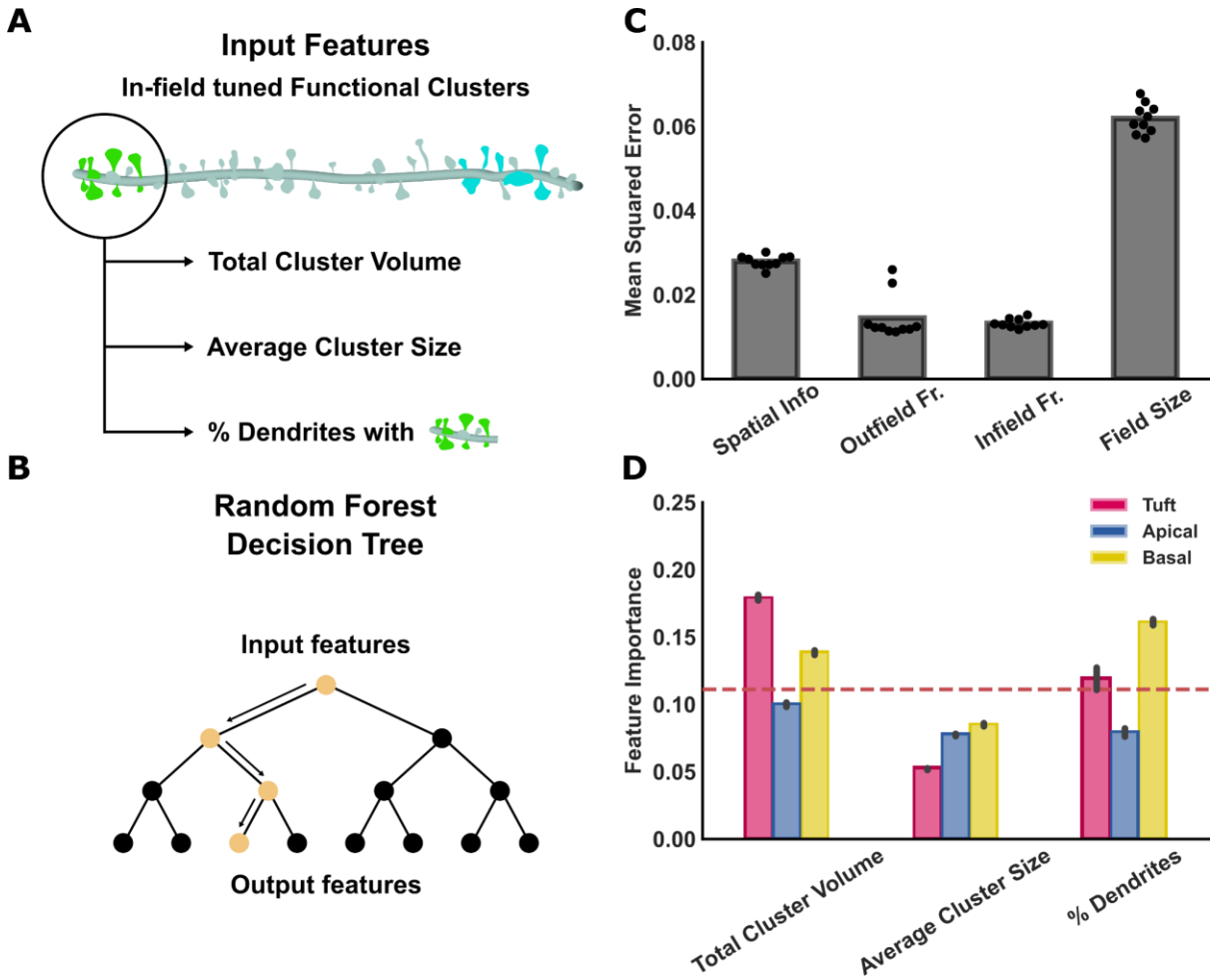

Figure 7: Cluster features Predict Spatial Tuning Quality *A.* Cluster features used as input to the multivariate random forest model to predict spatial tuning quality. The latter is assessed by the spatial information, out-field firing frequency, Infield firing frequency and field-size metrics. For each dendritic domain (Basal, Apical, and Tuft), cluster features include: the volume of in-field clusters, the size of in-field clusters, and the percentage of branches containing at least one in-field cluster. **B.** Schematic representation of the random forest methodology. The model combines predictions from multiple decision trees, each trained on subsets of the data (800 simulations used for training, 200 used for testing), to enhance robustness and accuracy in predicting model outputs. **C.** Mean Squared Error (MSE) of the output predictions on the testing set, providing a quantitative measure of the model's prediction accuracy. **D**. Feature importance in predicting simulation outputs for the Tuft, Apical, and Basal dendritic domains. The dashed line indicates the chance level of feature importance (~1.11). Error-bars represent the 95% confidence interval (CI) of the mean.

468 Together, these findings suggest that synaptic integration in spatially-tuned CA1 PNs is not
469 uniform across dendritic domains. The Tuft appears to capitalize on large, high-volume
470 clusters to initiate powerful nonlinear events, whereas the Basal domain favors a strategy of
471 parallelized integration across multiple dendrites to collectively drive somatic depolarization.
472 The apical domain's mechanisms remain more enigmatic, hinting at a rich, multidimensional
473 mode of integration that may involve other variables such as temporal coordination or dynamic
474 gating of the inhibitory inputs. These findings advance our understanding of how the
475 organization of synaptic inputs shapes neuronal processing and underscore the importance
476 of dendritic compartmentalization in spatial navigation.

477 Discussion

478 In this study, we combined high-resolution anatomical mapping with biophysical computational
479 modeling to investigate how the spatial distribution of excitatory synapses influences the
480 integrative properties of spatially-tuned CA1 PNs. Although the structural and
481 electrophysiological characteristics of these neurons have been well-documented *ex vivo*[8–10],
482 linking detailed anatomical properties of both E and I synapses to functional outcomes has
483 remained challenging. Our study reveals that excitatory synapses onto CA1 PNs are
484 organized in a non-uniform, domain-specific manner across the dendritic tree, and the
485 patterned activation of these synapses has a marked impact on the place-tuning properties of
486 these neurons.

487 Specifically, our comprehensive mapping of morphological and synaptic features reveals
488 marked differences in spine density between dendritic domains. In line with prior work, we
489 found that terminal dendrites exhibit a higher spine density compared to intermediate
490 dendrites, whereas inhibitory synapses are distributed uniformly throughout the dendritic tree[9].
491 As a result, the probability of finding spine clusters is much higher in terminal dendritic
492 compartments as opposed to intermediate ones. This disparity raises important questions
493 about the mechanisms that enable the preferential formation of spines toward terminal

494 regions. We propose that the smaller diameter and sealed ends of terminal dendrites lead to
495 elevated depolarization, thereby increasing the likelihood of synaptic plasticity events and
496 subsequent spine formation, a specialization that may enhance the neuron's ability to encode
497 spatial information[10,89,90]. This hypothesis is supported by prior modelling and experimental
498 work, whereby activation of inputs in terminal dendrites facilitates the induction of NMDA
499 spikes, resulting in persistent firing in L5 prefrontal cortical neuron models[91]. Similarly, in L2/3
500 pyramidal neurons of the primary visual cortex, NMDA spikes in the tuft dendrites facilitate
501 orientation tuning[92]. Models predict that such NMDA spikes are more effectively induced by
502 co-activated spines that are organized in clusters[93].

503 Previous studies inferred patterns of synaptic organization by analyzing E and I synaptic
504 density in individual branches and extrapolating respective distributions by multiplying
505 synaptic density to cumulated dendritic length[9]. Instead, our approach provides, for the first
506 time, a complete, neuron-wide reconstruction of E and I synapses in multiple mouse CA1 PNs,
507 as previously done for mouse layer 2/3 cortical PNs[42]. This unprecedented level of detail
508 allowed us to capture the full statistical distribution of synapses across entire dendritic trees,
509 revealing organizational principles that might have been overlooked in more localized
510 analyses. Prior work has focused primarily on identifying synaptic clusters by observing newly
511 formed spines during behavior[33,35,38]. These studies, while more relevant for linking synaptic
512 clustering to behavioral outcomes, lack accessibility to synaptic clustering at the whole-cell
513 level, as imaging techniques allow visualizing just a small proportion of dendrites *in vivo*. Our
514 dataset provides access to high-resolution anatomical features of all E and I synapses found
515 within all dendritic compartments of a CA1 PN. While providing only a static snapshot of
516 synaptic structure, it allows us to probe the functional impact of synaptic structure on single-
517 neuron computations, something not possible without this detailed information.

518 In addition to the structural mapping of E and I synaptic distribution across the entire dendritic
519 arbor, our work has generated heavily validated computational models of 5 different
520 reconstructed CA1 PNs using a common set of biophysical parameters. These models

521 account for both E and I synapse distributions and their respective input dynamics and serve
522 as powerful tools for investigating questions that go beyond place cell tuning. Several
523 important predictions came out of our models: first, we predict that place cells are more
524 efficiently generated (higher quality place tuning) when co-tuned inputs are delivered to
525 clusters of large spines. Indeed, randomizing the allocation of co-activated synapses -while
526 keeping their number, total volume or total strength fixed-, resulted in degraded place field
527 activity. This finding is likely due to enhanced signal propagation, reduced signal-to-noise and
528 increased energy efficiency by activating spines in clusters[41,94,95]. Achieving the same,
529 spatially-tuned, somatic output with small and randomly distributed synapses would require
530 more contacts, increasing energy consumption and reducing available space for additional
531 synapses[96,97]. This strategy aligns with principles of economical wiring and metabolic
532 efficiency, suggesting that neurons may have evolved to optimize both their structural and
533 functional features in order to better solve complex cognitive tasks[98].

534 Second, our models predict that the influence of synaptic clustering on neuronal spatial tuning
535 varies depending on the dendritic domain. While tuft dendrites may require larger clustered
536 synapses to impact somatic activity, in basal dendrites, distributed integration of multiple
537 clustered inputs plays a more important role. These observations are in line with studies
538 demonstrating strong compartmentalization of dendritic processing in CA1 PNs both *in*
539 *vitro*[68,85,99] and *in vivo*[14,100]. In particular, clusters of strong, NMDA-rich synapses primarily
540 found in the apical tuft, which are capable of generating plateau potentials, are more likely to
541 contribute to hippocampal feature selectivity during navigation than basal synapses[99–101]. The
542 activation of these large events is also known to initiate global plasticity events like the newly
543 found BTSP[102,102,103].

544 Notably, the proportion of basal dendrites containing in-field clusters emerged as the most
545 critical factor influencing spatial tuning. Previous studies have reported a strong correlation
546 between basal dendritic and somatic activity, suggesting that neurons parallelize basal inputs
547 to more efficiently regulate somatic output[14,104]. Additionally, the strong coupling between

basal dendrites and the soma may allow backpropagating action potentials to more effectively induce plastic changes, aligning basal dendritic tuning with somatic responses[14,105,106].

In sum, our results provide an integrated approach whereby detailed anatomical mapping and computational modeling are combined to unravel how E and I synaptic organization and its driving forces, which operate at the subcellular scale, shape cellular computations underlying spatial navigation. Specifically, it highlights the complex interplay between co-tuned activation of excitatory synapse clusters and dendritic domain properties in modulating place cell tuning. By linking such morphological features to computational outcomes, this work advances our understanding of the fundamental mechanisms through which structural and functional synaptic distributions modulate neuronal processing.

Resource availability

Lead contact

Further information and requests should be directed to and will be fulfilled by the lead contact, Panayiota Poirazi poirazi@imbb.forth.gr

Materials availability

This study did not generate new, unique reagents.

Data and code availability

The source code that generates all simulations and Figures, as well as the data that support this study will be freely available upon publication on GitHub.

Acknowledgments

We thank all members of the PoiraziLab for their valuable feedback on the project. This project has received funding from the European Union's Horizon 2020 research and innovation programme under the Marie Skłodowska-Curie grant agreement No.860949; Stavros Niarchos Foundation (SNF) and the Hellenic Foundation for Research and Innovation (H.F.R.I.) under the 5th Call of "Science and Society" Action Always strive for excellence – Theodoros Papazoglou" (Project Number: 28056); H.F.R.I call "Basic research Financing (Horizontal support of all Sciences)" under the National Recovery and Resilience Plan "Greece 2.0" funded by the European Union – NextGenerationEU (Project Number: 014941); COFLEX 14941 HFRI P.N. 80147/17.1.24; NIH grant No 1R01MH124867 to P.P.; NIH grants F31NS101820 and F32MH125600 to D.M.I.; NIH-NINDS (R35 NS127232) (FP), and an award

from the NOMIS Foundation (FP). A.L. is supported by National Institute of Mental Health (NIMH) R01MH124047 and R01MH124867; National Institute on Aging (NIA) RF1AG080818; National Institute of Neurological Disorders and Stroke (NINDS) Brain Initiative U01NS115530; NINDS R01NS121106, NINDS R01NS131728, and NINDS Brain Initiative R01NS133381

Author contributions

P.P., A.L., F.P., S.C., D.M.I., and S.T. conceived the study. D.M.I. performed the in-utero electroporation, prepared the tissue, and acquired the confocal images. L.H. developed a script enabling image deconvolution of the raw PN images. Y.K. and D.M.I. manually edited semi-automated synaptic reconstructions and participated in data analysis.

S.T. refined the morphological traces, developed and validated the model, implemented the simulation code, and analyzed the data. S.C. and S.T. generated the input patterns. S.T. wrote the manuscript, with editing support from P.P., A.L., F.P., S.C., and D.M.I.

Declaration of interests

The authors declare no competing interests.

Declaration of generative AI and AI-assisted technologies in the writing process

601 While preparing this work, the authors used large language models (ChatGPT-4o) for spelling
602 and grammar checks. The author(s) reviewed and edited the content as needed and take full
603 responsibility for the final publication.

604

605 ## Materials and Methods

606 ### Mice

607 All animals were handled according to protocols approved by the Institutional Animal Care and
608 Use Committee at Columbia University, New York. Postnatal day 98 C57BL/6 mice (strain
609 code: 000664; Jackson Laboratory) were used for all experiments. Timed-pregnant female
610 mice were maintained in a 12-hour light/dark cycle and obtained by overnight breeding with
611 males of the same strain. For timed-pregnant mating, noon after mating is considered E0.5.

612

613 ### Constructs

614 The tdTomato reporter was previously generated by the Polleux lab[42]. Briefly, the tdTomato
615 insert was subcloned into the pAAV-Ef1a-DIO eNpHR 3.0-EYFP plasmid (Addgene 26966)
616 between the AscI and NheI cloning sites. The inhibitory synapse reporter EGFP-Gephyrin
617 (clone P1) was obtained from H. Cline (TSRI, La Jolla, USA) and subcloned into the pUBC-
618 DIO Teal-Gephyrin plasmid (Addgene 73918) between the AscI and NheI cloning sites.

619

620 ### *In utero* electroporation

621 *In utero* electroporation targeting the dorsal hippocampus was performed using a triple-
622 electrode setup as previously described in E15.5 mouse embryos[13,107,108]. Endotoxin-free DNA

623 was injected using a glass pipette into one ventricle of the mouse embryos. Electroporation
624 was performed at E15.5 using a square wave electroporator (ECM 830, BTX) with two anodes
625 (positively charged) placed laterally on either side of the head and one cathode (negatively
626 charged) rostrally at a 0° angle to the horizontal plane. The electroporation settings were: 5
627 pulses of 40V for 50 ms with 500 ms intervals. Plasmids were used at the following
628 concentrations: Flex-tdTomato reporter plasmid: 1 µg/µl; Flex-EGFP-Gephyrin 0.45 µg/µl;
629 NLS-Cre recombinase: 150 pg/µl.

630

631 **Tissue preparation**

632 Animals at the indicated age were anaesthetized with isoflurane before intracardiac perfusion
633 with PBS and 4% PFA (Electron Microscopy Sciences). As previously described[42], 130 µm
634 coronal brain sections were obtained using a vibrating microtome (Leica VT1200S). Sections
635 were mounted on slides and briefly dehydrated at room temperature to reduce section
636 thickness before being coverslipped in Fluoromount-G (SouthernBiotech).

637

638 **Confocal imaging**

639 Confocal imaging was performed as previously described[42]. Briefly, images of electroporated
640 neurons in slices were acquired with a Nikon AXR confocal microscope equipped with a 100x,
641 1.49 NA Apochromat oil-immersion objective and controlled by NIS-Elements (Nikon
642 Instruments Inc., Melville, NY). Image volumes were acquired using galvano scanning with a
643 1024x1024 scan region, corresponding to a lateral pixel size of 110 nm and a z-step size of
644 100 nm. To compensate for signal attenuation caused by tissue scattering and spherical
645 aberration with increasing depth, laser power was linearly increased as a function of depth to
646 normalize the mean fluorescent intensity of pixels from image planes throughout the stack[42].
647 Following acquisition, image stacks were deconvolved using the GPU-based Richardson-Lucy

648 deconvolution algorithm within NIS-Elements. Deconvolution was performed with a theoretical
649 point spread function based on imaging acquisition parameters and used 20 iterations.
650 Individual z-stacks were subsequently stitched together using Fiji's Grid/Collection stitching
651 tool[109] to generate a single three-dimensional volume representing the entire neuron. Dendritic
652 spines and inhibitory synapses were quantified based on tdTomato fluorescence and EGFP-
653 Gephyrin puncta fluorescence, respectively. All quantifications were performed in CA1
654 hippocampus in sections of comparable rostro-caudal position.

655

656 **Neuron trace reconstruction**

657 Neuron traces, digital reconstructions of the dendritic tree, are an effective representation of
658 neuronal topology and geometry. The traces described using a tree graph and consist of 3-D
659 point coordinates, diameters, and connectivity between points. This representation enables
660 an extensive quantitative analysis of the geometrical organization of the neurons they
661 represent including total length, branching angles, distribution statistics and cumulative
662 distance from the soma[110]. In this paper, the initial reconstructions are obtained using the
663 automatic tracing methods built into the open-source 3D visualization and analysis tool
664 Vaa3D[45]. Then, experts manually proofread the traces and make adjustments with the built-in
665 proof-editing tools.

666

667 **Synapse detection**

668 Excitatory and inhibitory synapses were annotated with the Spine Detector and IS Detector
669 toolkits within Vaa3D software as previously described[42]. Briefly, excitatory synapses are
670 identified as dendritic spines segmented by the Spine Detector toolkit using the image and
671 neuron trace as inputs[111,112]. Because the dendrite traces represent the dendrites with a series
672 of overlapping nodes[113], information about the volume and distance from the dendrite of each

673 spine can be associated with its nearest node to assign a location within the spatial context of
674 the dendritic arbor. Users have the ability to accept or reject potential spines and adjust their
675 volume.

676 We labeled inhibitory synapses using the scaffolding protein Gephyrin tagged with EGFP as
677 a marker[114]. Because these synapses can only occur on the dendrites or the spines of neurons
678 of interest, IS Detector uses the image from the cell-fill channel containing the dendrites and
679 the spines as a mask image to extract the relevant region for the inhibitory synaptic marker.
680 Then, signal beyond user-input parameters for minimum/maximum voxel count and distance
681 from the trace is excluded and potential inhibitory synapses from the resulting image are
682 identified based on a user-input intensity threshold. Users have the ability to accept or reject
683 potential inhibitory synapses, adjust their volume, and assign them as dendrite-targeting or
684 spine-targeting.

685

686 **Dendritic diameter correction**

687 To improve the accuracy of the morphological data and ensure the physiological plausibility of
688 the neuronal reconstructions, a custom smoothing algorithm was applied to correct artifactual
689 fluctuations in dendritic diameters (**Figure S1**). This algorithm utilized a weighted moving
690 average filter to smooth out large changes in diameter while preserving the overall structural
691 integrity of the neuron. The filter was designed to account for local variations in diameter by
692 applying larger weight to nearby points, reducing the influence of outliers and providing a
693 consistent tapering pattern along the dendrites.

694 Prior to smoothing algorithm, a minimum diameter threshold was applied to all diameters to
695 address the occurrence of bottlenecks. These bottlenecks could significantly impact
696 simulations by increasing the axial resistance and altering signal propagation. The minimum

697 diameter threshold was domain-specific, reflecting the physiological constraints of different
698 neuronal compartments.

699 Synaptic distribution analysis

700 *Synaptic null distribution: within-domain and within-subdomain randomization*

701 For each reconstructed morphology, synapses were randomly reassigned within branches of
702 the same domain or sub-domain, ensuring a uniform probability distribution. Specifically, we
703 first extracted the nodes of interest from the reconstructed arbor trace and then reassigned
704 the annotations describing spine features to new, randomly selected locations within the same
705 domain. This process preserved the overall structure of the arbor while randomizing synaptic
706 positions. We repeated this procedure 1,000 times to create the null distribution, conducting
707 the necessary analysis on each randomized dataset.

708 *Structural cluster analysis*

709 Putative structural clusters were identified using a hierarchical clustering algorithm applied
710 solely to large spines, i.e., those above the 80th percentile of the spine volume distribution.
711 For each branch, we selected the large spines and clustered them based on their relative
712 distance from the soma (i.e., path length). Specifically, we used the SciPy hierarchical
713 clustering linkage with *complete* method to calculate the Euclidian distance. A threshold of 10
714 micrometers was then used to define clusters, after which we collected their characteristics
715 (e.g., spine count, total volume). Since the clustering was performed separately for each
716 branch, any potential clusters spanning branching points were excluded from the analysis.

717 Computational Modeling

718 The CA1 PN models, implemented using the Python version of the NEURON simulation
719 environment[67], and were inspired by prior work by using the ionic mechanism and their
720 distribution throughout the dendrosomatic axis[26]. The ionic channels, written using NMODL

language, used for this project include: inward transient sodium current (I_{Na}), outward delayed rectifier potassium current (I_{Kdr}), A-type potassium current (I_A), Sodium persistent current (I_{Nap}), Hyperpolarization-activated current (I_h), Slowly activating muscarinic potassium current (I_m), Calcium current from T-type channel (I_{CaT}), Calcium current from L-type channel (I_{CaL}), Calcium current from R-type channel (I_{CaR}), Slow calcium-dependent potassium current (I_{sAHP}), Medium calcium-dependent potassium current (I_{mAHP}). Minor modifications were implemented in the kinetics and distribution of some channels. To facilitate the rapid and reproducible generation of models, we developed a Python Class capable of processing neuronal morphologies in .swc file format and automatically incorporating the appropriate biophysical properties and channel distributions.

To ensure high spatial resolution in the simulations, we determined the number of segments ($\mathrm{n_{seg}}$) for each neuronal section using the lambda rule, which is based on the Alternating Current (AC) length constant (λ). A ten-fold higher frequency was used in the calculation to obtain a finer spatial discretization of each section. Specifically, we employed the following equation (Eq. 1):

$$\mathrm{n_{seg}} = 2 \cdot \left\lfloor \frac{\frac{L}{d_\lambda \cdot \lambda_f} + 0.999}{2} \right\rfloor + 1 \quad (1)$$

where L is the length of the section, d_λ the fraction of the AC length constant (typically 0.1), λ_f ***f*** the AC length constant at the chosen frequency f, and $\lfloor\cdot\rfloor$ denotes a function that converts a specified value into an integer number. This approach ensured that all segments were small enough to disentangle inputs coming from most of nearby synapse couples, providing accurate spatial and biophysical representation of the model.

Modeling Synapses

744 We incorporated both glutamatergic (excitatory) and GABAergic (inhibitory) synapses. All
745 dendritic spines identified in the reconstructed neurons were assumed to be excitatory
746 synapses containing both AMPA and NMDA receptors, while inhibitory synapses were
747 modeled as $GABA_A$-mediated inputs. Synaptic strength was adjusted based on the synapse
748 size measured from the original reconstruction and, for a subset of excitatory synapses, by
749 the distance from the soma. Specifically, for excitatory synapses, validated conductance
750 values for both NMDAR and AMPAR components were first calculated. The AMPA
751 conductance was then scaled by a volume-dependent scaling factor (Eq. 2). Both AMPA and
752 NMDA components for synapses in Basal, Trunk and Oblique compartments were further
753 adjusted by a distance-dependent scaling factor[71,73]. In contrast, inhibitory synapses were
754 scaled solely by the volume-dependent factor (Eq. 3).

755 $$AMPA\ Volume\ scaling = 0.6 \cdot \frac{Spine\ volume_i}{Average\ spine\ volume} + 0.4 \quad (2)$$

756 $$GABA\ Volume\ scaling = \frac{PSD\ volume_i}{Average\ PSD\ volume} \quad (3)$$

757

758 ***AMPA & $GABA_A$ definition***

759 AMPA and $GABA_A$ synapses were simulated with a two-state kinetic model, defined by rise
760 and decay times. The synaptic current is calculated according to the following equations (Eqs.
761 4, 5):

762 $$I_{syn} = \mathrm{g}_{syn}(t) \cdot (V_m - E_{syn}), syn \in \{\mathrm{AMPA}, \mathrm{GABA_A}\} \quad (4)$$
763
764
765 $$\mathrm{g}_{syn}(t) = f_{norm} \cdot \bar{\mathrm{g}}_{peak} \cdot \left(\exp\left(-\frac{t}{\tau_d}\right) - \exp\left(-\frac{t}{\tau_r}\right)\right) \quad (5)$$

766 where I_{syn} is the synaptic current, V_m the membrane potential, g_{syn} the receptor conductance,
767 g_{peak} the peak conductance and E_{syn} its reverse potential. τ_r and τ_d represent the rise and

768 decay time constants, respectively. The factor f_{norm} normalizes the difference of exponentials
769 so that the peak of g_{syn} equals $\bar{g}_{peak}$ and its calculated using the formula below (Eq. 6).

770 $$f_{norm} = \frac{1}{g_{syn}(t_{peak})}, t_{peak} = \frac{\tau_d \tau_r}{\tau_d - \tau_r} \ln \frac{\tau_d}{\tau_r} \quad (6)$$

771

772

773 ***NMDA definition***

774 The NMDA component of the excitatory synapses was also simulated as a two-state kinetic
775 model but with an additional factor that accounts for the voltage dependent removal of the
776 Magnesium blockage. The mechanism is described by the following equations (Eqs. 7, 8):

777 $$I_{NMDA} = g_{NMDA}(t) \cdot h(V_m) \cdot (V_m - E_{NMDA}) \quad (7)$$
778

779

780 $$h(V_m) = \frac{1}{1 + \eta [\mathrm{Mg}^{2+}]_o \exp\left(-\gamma\left(V_m - V_{half}\right)\right)} \quad (8)$$

781 where $h(\cdot)$ is a sigmoid function, η denotes the Magnesium sensitivity of unblock, $[\mathrm{Mg}^{2+}]_o$ the
782 Magnesium extracellular concentration, γ the slope factor that determines how steep the
783 transition is around the midpoint, and V_{half} the membrane potential of the midpoint of the
784 sigmoid. $g_{NMDA}(t)$ is calculated with the same equations as the other synaptic currents (Eqs.
785 5, 6).

786 **Pyramidal neuron model validation**

787 The parameters that defined the biophysical properties and channel distributions were
788 carefully validated to match the cell's behavior with experimental data. We ensured that using
789 the same values for all morphologies would still adhere to the experimental values for each
790 cell, while also introducing variability expected in a heterogeneous population of pyramidal

neurons. We used hyperpolarizing step current sweeps to validate passive properties as the input resistance ($\mathrm{R_{in}}$), membrane time constant (τ_m), sag ratio and the dendritic attenuation, following the protocols illustrated in **Magee (1998)**[68]**, Golding et al. (2005)**[69] for the voltage attenuation and **Masurkar et al. (2020)**[8] for $\mathrm{R_{in}}$, τ_m and sag ratio. We then used a depolarizing step current sweeps to validate the frequency-input (F-I) curve and the adaptation from **Masurkar et al. (2020)**[8]. For the synaptic strength validation, we followed the protocol used in **Magee and Cook, 2000**[71], stimulating average size synapses at increasing distance from the soma and maintaining the 0.2 mV somatic depolarization observed experimentally.

Inputs design

Grid-like and Place-like inputs

In accordance with the formulation described in **Shuman et al. (2020)**[115], entorhinal cortex layer III (ECIII) grid-like inputs were modeled as the summation of three sinusoidal wave components, following the approach of **Solstad et al. (2006)**[116]. In contrast, place-like inputs from CA3 were generated by integrating these grid-like inputs. Specifically, grid-cell activity was represented as the sum of three two-dimensional sinusoidal gratings, each defined by a distinct wave vector. The resulting grid-like function was computed as (Eq. 9):

$$\mathrm{g}_w(x,y) = \frac{2}{3}\left(\frac{1}{3}\sum_{i=1}^{3}\cos\left(k_i\,(r-r_0)\right)+\frac{1}{2}\right) \quad (9)$$

where the parameter set $w = (\lambda, \theta, r_0)$ defines the grid spacing λ, orientation θ, and the spatial location of a theoretical place cell $r_0 = [x_0, y_0]^{\mathrm{T}}$, while the variable $r = [x, y]^{\mathrm{T}}$ represents the current position, and k denotes the wave vectors arranged at angular intervals of $\frac{\pi}{3}$ and $\frac{2\pi}{3}$, respectively (Eq. 10).

$$k_i = \frac{1}{\lambda}\left[\cos\left(\theta + (i-1)\frac{\pi}{3}\right), \sin\left(\theta + (i-1)\frac{\pi}{3}\right)\right]^{\mathrm{T}} \quad (10)$$

These grid-like functions were used to compute the probability of spike generation as a function of the animal's position and the theoretical place fields. To incorporate theta rhythmic modulation, a sinusoidal filter was applied to these probabilities (Eq 11):

$$p(t) = \mathrm{g}_w(x,y)\frac{\sin\left(2\pi \cdot f_\theta \cdot \left(\frac{t}{1000}\right) + \varphi_{theta}\right) + 1}{2} \quad (11)$$

where $f_\theta = 8\mathrm{Hz}$ and $\phi_\theta = 0^o$ correspond to the theta-cycle frequency and phase, respectively, and t is expressed in milliseconds. A spike was generated for a given grid cell whenever $p(t)$ exceeded a random value sampled from a normal distribution with mean $\mu = 0.7$ and standard deviation $\sigma = 0.05$ or a random value from a uniform distribution used to introduce baseline noise. This process was repeated across all grid-like cells to construct the entire set of theoretical place fields.

To model CA3 place-like inputs, we combined the generated grid-like fields from EC inputs, ensuring proper gamma filtering and theta-phase locking. Similarly to EC inputs, a spike was generated when the probability $p(t)$ was greater than a normally distributed threshold value or a noise baseline. Additionally, a 17 ms delay was introduced to account for the natural temporal delay between EC and CA3 input streams. Finally, each spike train was filtered to a function that simulate the effect of synaptic failure based on published data[117].

Noisy inputs

To account for non-place-tuned inputs, we generated a set of noisy inputs modeled as Poisson-distributed spike trains with low baseline firing rates. To introduce temporal fluctuations, these spike trains were modulated by applying a Gaussian filter at randomly selected time points, transiently increasing the firing rate. In our approach, the probability for a spike to occur was (Eq. 12):

837 $$p(t) = O + H \cdot \exp\left(\frac{\left(t - t_{peak}\right)^2}{2\sigma^2}\right) \quad (12)$$

838 where O represents the baseline offset of the gaussian curve, H is the peak amplitude, t is the
839 time at which the spike occurred and t_{peak} is a randomly chosen value corresponding to the
840 mean value of the Gaussian filter. The standard deviation σ is also chosen randomly in a fixed
841 window of values (400 ms, 720 ms) and represents the width of the window with slightly higher
842 firing frequency.

843 This process ensured that noisy inputs exhibited sporadic increases of activity while
844 maintaining an overall unstructured firing pattern, effectively capturing the background
845 synaptic activity present in the hippocampal CA1 place cells. Similarly to place tuned inputs,
846 the noisy spike trains were further processed to account for synaptic failure.

847

848 ***Inhibitory inputs***

849 Inhibitory inputs were modeled as theta-modulated, gamma-filtered Poisson-distributed spike
850 trains, with firing properties tailored to different interneuron subtypes as described in **Bezaire**
851 **et al., 2016**[76]. To generate these spike trains, we set baseline firing rates according to known
852 physiological values for each interneuron type. These spike trains were then filtered using a
853 theta-modulated function, ensuring that their activity exhibited phase locking to the theta cycle
854 at subtype-specific phases (Eq. 11).

855 Additionally, a gamma-frequency filtering step was applied to refine the temporal structure of
856 the remaining spikes. The level of randomness was controlled by introducing a noise
857 parameter, which varied across interneuron types to reflect their intrinsic firing variability.
858 Delays of 300 ms were incorporated to approximate transmission latencies. Specifically, inputs
859 were tuned to replicate the activity of different interneurons neurogliaform (NGF) cells, oriens-
860 lacunosum moleculare (OLM) cells, parvalbumin-expressing basket (PVbasket) cells, apical

861 dendrite targeting cholecystokinin-expressing (CCK) cells, Bistratified cells, and Ivy cells with
862 peak firing rates ranging from 2.8 Hz to 30 Hz, distinct theta-phase preferences, and varying
863 degrees of noise, capturing the diversity of inhibitory influences in the hippocampal network.

864

865 **Input distribution**

866 Synaptic inputs were distributed in an anatomically accurate manner. For inhibitory synapses,
867 their connection probabilities to each interneuron subtype were based on estimates from
868 **Bezaire and Soltesz (2013)**[118], with slight upward adjustments to account for missing
869 interneuron types. While NGF and OLM inputs were uniformly distributed across tuft synapses,
870 the distribution of other interneurons followed a nonlinear function of the distance from the
871 soma. This distribution pattern was informed by anatomical observations while maintaining
872 symmetry between the apical and basal dendritic domains. Specifically, PV basket synapses
873 were concentrated near the soma, while CCK and Ivy cells targeted more distal synapses in
874 the apical and basal domains, respectively. Bistratified cell synapses were predominantly
875 located in the middle regions of both domains (**Figure S2**).

876 ECIII grid-like inputs were directed to synapses on the tuft dendrites in the stratum lacunosum-
877 moleculare, whereas CA3 place-like inputs primarily targeted synapses in the trunk, oblique,
878 and basal dendritic domains, spanning the stratum oriens and stratum radiatum. At the branch
879 level, place-tuned inputs were assigned to both clustered and dispersed synapses. Using
880 GluSnFR-based experimental data from **Adoff et al. (2021)**[39] as a reference, we determined
881 the probability of each synapse to receive place-tuned inputs, guided by the observed ratios
882 of clustered vs. dispersed synapses and the relative distributions in the apical vs. basal
883 domains.

884 The total number of activated clustered synapses, tuned to the somatic place field, was
885 randomly determined using a transformation of a Gaussian-distributed variable (Eq. 13):

$$n_{in} = r \cdot \frac{n_{cs}}{n_{pf}}, r = 0.9 + \frac{z^{1.5}}{3} \quad (13)$$

Where n_{in} represents the number of clustered in-field tuned synapses, n_{cs} and n_{pf} represent the number of clustered synapses and the number of place fields, respectively. z is a normally distributed random variable with mean 0 and standard deviation 1, so that $z \sim \mathcal{N}(0,1)$, keeping only the positive values. The range r is limited to values lower than 1.6.

The Gaussian shape was chosen to replicate the distribution of place field properties observed at the population level by **Mizuseki et al. (2012)**[84]. Clustered synapses assigned to the remaining 11 place fields were selected randomly with a fixed probability of (Eq. 14):

$$n_{out} = 0.4 \cdot \frac{n_{cs}}{n_{pf}} \quad (14)$$

Where n_{out} is the number of clustered out-field tuned synapses. Dispersed synapses were also randomly selected with fixed probabilities, determining whether they would receive place-tuned or noisy inputs. To account for biological variability, we generated a set of 1,000 distinct connectivity patterns for each of the five morphologies, ensuring a realistic representation of network heterogeneity.

Inputs Shuffling

To investigate the role of synaptic clustering in shaping neuronal responses, we implemented three distinct synaptic input shuffling protocols that redistributed the incoming place-tuned inputs while preserving specific structural or functional properties of the original configuration. In the Shuffled – Same Number (SSN) condition, for each dendritic domain, we first computed the number of synapses activated in the control (i.e., clustered) configuration. The same input patterns were then reassigned to an equal number of randomly selected synapses within the same domain, thereby preserving synapse count but disrupting spatial clustering.

In the Shuffled – Same Volume (SSV) protocol, we calculated the total volume of all synapses activated per place field in the control configuration. Synaptic locations were then randomly selected until their cumulative volume matched that total volume. As this procedure typically resulted in a greater number of activated synapses, due to the inclusion of smaller synapses, the set of input spike trains used was expanded by sampling from the pool of inputs applied in the original, clustered configuration.

The Shuffled – Same Weight (SSW) protocol further refined this approach by summing the total synaptic weight from the control configuration, accounting for both the synaptic volume and the synaptic democracy principle (i.e., equalization of synaptic impact regardless of location). Synapses were then randomly selected until their combined weights matched the original total. Although this method also led to an increased number of activated synapses compared to the control, the number was lower than that observed in the SSV condition.

Place cell quantification

To quantify the spatial tuning properties of the simulated neurons, we computed the firing rate maps for each cell across the linear track, and used them to calculate the various place field features. The Field Size identifies the spatial extent of contiguous bins around the peak firing location where the firing rate remains above a given relative threshold. Once the Place Field width was characterized, we determined the mean firing rate within and outside the identified field region, respectively named In-field and Out-field Firing Frequency, respectively. In addition, spatial selectivity was assessed using a modified version of the spatial information index[83]. This metric calculates the information content of firing in bits per second by comparing the firing rate in each spatial bin to the mean firing rate across the track, weighted by occupancy probability, i.e., time spent in each spatial bin. The time spent in each bin was used to normalize firing rates, and the spatial information was computed (Eq. 15) as:

$$Spatial\ Info = \sum_{i=1}^{N_{bins}} p_i \cdot \frac{\lambda_i}{\lambda} \cdot \log_2\left(\frac{\lambda_i}{\lambda}\right) \quad (15)$$

Where p_i is the occupancy probability of bin i, λ_i is the firing rate in that bin and λ is the mean firing rate across all bins, N_{bins}.

Multivariate Random Forest

To assess whether the structural features of synaptic clusters could predict the functional output of the simulated neurons, we employed a supervised machine learning approach using a Random Forest regression model. Specifically, we trained a multi-output regression model to predict place field properties (i.e., Spatial Information, In-field and Out-of-field Firing Frequency, and Field Size) from cluster-derived input features (i.e., total in-field cluster volume, average in-field cluster size, and the proportion of dendritic branches containing in-field clusters). These features were normalized to [0,1] range using a Min-Max Scaler to ensure comparability across dimensions. The target output matrix comprised the aforementioned spatial metrics, which were likewise scaled prior to training. For the analysis we used simulations conducted under the Control allocation protocol, excluding those that exhibited overflow or contained missing values.

We used a Multi-Output Regressor wrapping a Random Forest Regressor (100 estimators per model). Models were trained and evaluated over 10 independent runs using an 80/20 train-test split, with mean squared error used to assess performance across both individual outputs and overall predictions. Control protocols were validated against two baselines: one involving permutation of the input features (Random training inputs, not shown) and another involving selective removal of key input features (Removal input feature, not shown) to confirm the robustness and informativeness of the cluster descriptors. Feature importance values were computed as the average importance across all estimators within the ensemble.

SHAP-Based Feature Attribution Analysis

To investigate the contribution of synaptic cluster features to the spatial coding properties of simulated neurons, we employed SHAP (*SHapley Additive exPlanations*), a game-theory approach for interpreting machine learning models[88]. We computed SHAP values using the *TreeExplainer* provided by the SHAP Python library, which is optimized for tree-based models. SHAP values were calculated on the training set to ensure consistency with the model fitting. The *summary_plot()* function was used to visualize both the magnitude and direction of each feature's effect. Feature values were color-coded to indicate their relative magnitude (red for high values, blue for low values), enabling intuitive interpretation of whether increasing a specific feature tended to increase or decrease a given output.

To complement the qualitative visual inspection, we also computed the Pearson correlation between feature values and their corresponding SHAP values. This provided a numerical estimate of the directionality and strength of influence each feature exerted on the model output.

Simulation environment and statistical analysis

All simulations were performed on our High-Performance Computing Cluster (Rocks 7.0) with 624 cores and 3.328 TB of shared RAM under CentOS 7.4 OS[119], through the NEURON simulator[120] using Python via an Anaconda virtual environment. Neuronal models have been simulated at a sampling rate of 40 kHz (dt = 0.025 ms). For all standard statistical tests (detailed in all relevant figure legends), the α was chosen to be 0.05 for statistical significance. To correct for multiple comparisons, the α was divided by the number of tests according to the Bonferroni's procedure. Throughout the figures, p values are denoted by * ($p < 0.05$), ** ($p < 0.01$), and *** ($p < 0.001$).

References

1. O'Keefe, J., and Dostrovsky, J. (1971). The hippocampus as a spatial map. Preliminary evidence from unit activity in the freely-moving rat. Brain Res *34*, 171–175. https://doi.org/10.1016/0006-8993(71)90358-1.

2. Muller, R.U., and Kubie, J.L. (1987). The effects of changes in the environment on the spatial firing of hippocampal complex-spike cells. J Neurosci *7*, 1951–1968. https://doi.org/10.1523/JNEUROSCI.07-07-01951.1987.

3. Quirk, G.J., Muller, R.U., and Kubie, J.L. (1990). The firing of hippocampal place cells in the dark depends on the rat's recent experience. J Neurosci *10*, 2008–2017. https://doi.org/10.1523/JNEUROSCI.10-06-02008.1990.

4. Bostock, E., Muller, R.U., and Kubie, J.L. (1991). Experience-dependent modifications of hippocampal place cell firing. Hippocampus *1*, 193–205. https://doi.org/10.1002/hipo.450010207.

5. Leutgeb, S., Leutgeb, J.K., Barnes, C.A., Moser, E.I., McNaughton, B.L., and Moser, M.-B. (2005). Independent codes for spatial and episodic memory in hippocampal neuronal ensembles. Science *309*, 619–623. https://doi.org/10.1126/science.1114037.

6. Turi, G.F., Li, W.-K., Chavlis, S., Pandi, I., O'Hare, J., Priestley, J.B., Grosmark, A.D., Liao, Z., Ladow, M., Zhang, J.F., et al. (2019). Vasoactive Intestinal Polypeptide-Expressing Interneurons in the Hippocampus Support Goal-Oriented Spatial Learning. Neuron *101*, 1150-1165.e8. https://doi.org/10.1016/j.neuron.2019.01.009.

7. Zutshi, I., Valero, M., Fernández-Ruiz, A., and Buzsáki, G. (2022). Extrinsic control and intrinsic computation in the hippocampal CA1 circuit. Neuron *110*, 658-673.e5. https://doi.org/10.1016/j.neuron.2021.11.015.

8. Masurkar, A.V., Tian, C., Warren, R., Reyes, I., Lowes, D.C., Brann, D.H., and Siegelbaum, S.A. (2020). Postsynaptic integrative properties of dorsal CA1 pyramidal neuron subpopulations. J Neurophysiol *123*, 980–992. https://doi.org/10.1152/jn.00397.2019.

9. Megías, M., Emri, Z., Freund, T.F., and Gulyás, A.I. (2001). Total number and distribution of inhibitory and excitatory synapses on hippocampal CA1 pyramidal cells. Neuroscience *102*, 527–540. https://doi.org/10.1016/s0306-4522(00)00496-6.

10. Spruston, N. (2008). Pyramidal neurons: dendritic structure and synaptic integration. Nat Rev Neurosci *9*, 206–221. https://doi.org/10.1038/nrn2286.

11. Dougherty, K.A., Islam, T., and Johnston, D. (2012). Intrinsic excitability of CA1 pyramidal neurones from the rat dorsal and ventral hippocampus. J Physiol *590*, 5707–5722. https://doi.org/10.1113/jphysiol.2012.242693.

12. Sheffield, M.E.J., Adoff, M.D., and Dombeck, D.A. (2017). Increased Prevalence of Calcium Transients across the Dendritic Arbor during Place Field Formation. Neuron *96*, 490-504.e5. https://doi.org/10.1016/j.neuron.2017.09.029.

13. Blockus, H., Rolotti, S.V., Szoboszlay, M., Peze-Heidsieck, E., Ming, T., Schroeder, A., Apostolo, N., Vennekens, K.M., Katsamba, P.S., Bahna, F., et al. (2021). Synaptogenic

activity of the axon guidance molecule Robo2 underlies hippocampal circuit function. Cell Rep *37*, 109828. https://doi.org/10.1016/j.celrep.2021.109828.

14. O'Hare, J.K., Gonzalez, K.C., Herrlinger, S.A., Hirabayashi, Y., Hewitt, V.L., Blockus, H., Szoboszlay, M., Rolotti, S.V., Geiller, T.C., Negrean, A., et al. (2022). Compartment-specific tuning of dendritic feature selectivity by intracellular Ca2+ release. Science *375*, eabm1670. https://doi.org/10.1126/science.abm1670.

15. Amaral, D.G., and Witter, M.P. (1989). The three-dimensional organization of the hippocampal formation: a review of anatomical data. Neuroscience *31*, 571–591. https://doi.org/10.1016/0306-4522(89)90424-7.

16. Suh, J., Rivest, A.J., Nakashiba, T., Tominaga, T., and Tonegawa, S. (2011). Entorhinal cortex layer III input to the hippocampus is crucial for temporal association memory. Science *334*, 1415–1420. https://doi.org/10.1126/science.1210125.

17. Larkum, M. (2013). A cellular mechanism for cortical associations: an organizing principle for the cerebral cortex. Trends Neurosci *36*, 141–151. https://doi.org/10.1016/j.tins.2012.11.006.

18. Xu, N., Harnett, M.T., Williams, S.R., Huber, D., O'Connor, D.H., Svoboda, K., and Magee, J.C. (2012). Nonlinear dendritic integration of sensory and motor input during an active sensing task. Nature *492*, 247–251. https://doi.org/10.1038/nature11601.

19. Takahashi, H., and Magee, J.C. (2009). Pathway interactions and synaptic plasticity in the dendritic tuft regions of CA1 pyramidal neurons. Neuron *62*, 102–111. https://doi.org/10.1016/j.neuron.2009.03.007.

20. Magee, J.C. (2000). Dendritic integration of excitatory synaptic input. Nat Rev Neurosci *1*, 181–190. https://doi.org/10.1038/35044552.

21. Tzilivaki, A., Kastellakis, G., Schmitz, D., and Poirazi, P. (2022). GABAergic Interneurons with Nonlinear Dendrites: From Neuronal Computations to Memory Engrams. Neuroscience *489*, 34–43. https://doi.org/10.1016/j.neuroscience.2021.11.033.

22. Katz, Y., Menon, V., Nicholson, D.A., Geinisman, Y., Kath, W.L., and Spruston, N. (2009). Synapse distribution suggests a two-stage model of dendritic integration in CA1 pyramidal neurons. Neuron *63*, 171–177. https://doi.org/10.1016/j.neuron.2009.06.023.

23. Branco, T., and Häusser, M. (2010). The single dendritic branch as a fundamental functional unit in the nervous system. Curr Opin Neurobiol *20*, 494–502. https://doi.org/10.1016/j.conb.2010.07.009.

24. Losonczy, A., and Magee, J.C. (2006). Integrative properties of radial oblique dendrites in hippocampal CA1 pyramidal neurons. Neuron *50*, 291–307. https://doi.org/10.1016/j.neuron.2006.03.016.

25. Gasparini, S., and Magee, J.C. (2006). State-dependent dendritic computation in hippocampal CA1 pyramidal neurons. J Neurosci *26*, 2088–2100. https://doi.org/10.1523/JNEUROSCI.4428-05.2006.

26. Poirazi, P., Brannon, T., and Mel, B.W. (2003). Arithmetic of subthreshold synaptic summation in a model CA1 pyramidal cell. Neuron *37*, 977–987. https://doi.org/10.1016/s0896-6273(03)00148-x.

1065 27. Polsky, A., Mel, B.W., and Schiller, J. (2004). Computational subunits in thin dendrites
1066 of pyramidal cells. Nat Neurosci *7*, 621–627. https://doi.org/10.1038/nn1253.

1067 28. Cichon, J., and Gan, W.-B. (2015). Branch-specific dendritic Ca(2+) spikes cause
1068 persistent synaptic plasticity. Nature *520*, 180–185.
1069 https://doi.org/10.1038/nature14251.

1070 29. Tzilivaki, A., Kastellakis, G., and Poirazi, P. (2019). Challenging the point neuron
1071 dogma: FS basket cells as 2-stage nonlinear integrators. Nat Commun *10*, 3664.
1072 https://doi.org/10.1038/s41467-019-11537-7.

1073 30. Mel, B. (1991). The Clusteron: Toward a Simple Abstraction for a Complex Neuron. In
1074 Advances in Neural Information Processing Systems (Morgan-Kaufmann).

1075 31. Mel, B.W., Ruderman, D.L., and Archie, K.A. (1998). Translation-invariant orientation
1076 tuning in visual “complex” cells could derive from intradendritic computations. J
1077 Neurosci *18*, 4325–4334. https://doi.org/10.1523/JNEUROSCI.18-11-04325.1998.

1078 32. Poirazi, P., and Mel, B.W. (2001). Impact of active dendrites and structural plasticity on
1079 the memory capacity of neural tissue. Neuron *29*, 779–796.
1080 https://doi.org/10.1016/s0896-6273(01)00252-5.

1081 33. Fu, M., Yu, X., Lu, J., and Zuo, Y. (2012). Repetitive motor learning induces
1082 coordinated formation of clustered dendritic spines in vivo. Nature *483*, 92–95.
1083 https://doi.org/10.1038/nature10844.

1084 34. Oh, W.C., Parajuli, L.K., and Zito, K. (2015). Heterosynaptic structural plasticity on local
1085 dendritic segments of hippocampal CA1 neurons. Cell Rep *10*, 162–169.
1086 https://doi.org/10.1016/j.celrep.2014.12.016.

1087 35. Frank, A.C., Huang, S., Zhou, M., Gdalyahu, A., Kastellakis, G., Silva, T.K., Lu, E.,
1088 Wen, X., Poirazi, P., Trachtenberg, J.T., et al. (2018). Hotspots of dendritic spine
1089 turnover facilitate clustered spine addition and learning and memory. Nat Commun *9*,
1090 422. https://doi.org/10.1038/s41467-017-02751-2.

1091 36. Takahashi, N., Kitamura, K., Matsuo, N., Mayford, M., Kano, M., Matsuki, N., and
1092 Ikegaya, Y. (2012). Locally synchronized synaptic inputs. Science *335*, 353–356.
1093 https://doi.org/10.1126/science.1210362.

1094 37. Kastellakis, G., Silva, A.J., and Poirazi, P. (2016). Linking Memories across Time via
1095 Neuronal and Dendritic Overlaps in Model Neurons with Active Dendrites. Cell Rep *17*,
1096 1491–1504. https://doi.org/10.1016/j.celrep.2016.10.015.

1097 38. Sehgal, M., Filho, D.A., Kastellakis, G., Kim, S., Lee, J., Shen, Y., Huang, S., Lavi, A.,
1098 Fernandes, G., Davila Mejia, I., et al. (2025). Compartmentalized dendritic plasticity in
1099 the mouse retrosplenial cortex links contextual memories formed close in time. Nat
1100 Neurosci *28*, 602–615. https://doi.org/10.1038/s41593-025-01876-8.

1101 39. Adoff, M.D., Climer, J.R., Davoudi, H., Marvin, J.S., Looger, L.L., and Dombeck, D.A.
1102 (2021). The functional organization of excitatory synaptic input to place cells. Nat
1103 Commun *12*, 3558. https://doi.org/10.1038/s41467-021-23829-y.

1104 40. Hwang, F.-J., Roth, R.H., Wu, Y.-W., Sun, Y., Kwon, D.K., Liu, Y., and Ding, J.B.
1105 (2022). Motor learning selectively strengthens cortical and striatal synapses of motor

engram neurons. Neuron *110*, 2790-2801.e5. https://doi.org/10.1016/j.neuron.2022.06.006.

41. Kastellakis, G., Cai, D.J., Mednick, S.C., Silva, A.J., and Poirazi, P. (2015). Synaptic clustering within dendrites: an emerging theory of memory formation. Prog Neurobiol *126*, 19–35. https://doi.org/10.1016/j.pneurobio.2014.12.002.

42. Iascone, D.M., Li, Y., Sümbül, U., Doron, M., Chen, H., Andreu, V., Goudy, F., Blockus, H., Abbott, L.F., Segev, I., et al. (2020). Whole-Neuron Synaptic Mapping Reveals Spatially Precise Excitatory/Inhibitory Balance Limiting Dendritic and Somatic Spiking. Neuron *106*, 566-578.e8. https://doi.org/10.1016/j.neuron.2020.02.015.

43. Atasoy, D., Aponte, Y., Su, H.H., and Sternson, S.M. (2008). A FLEX switch targets Channelrhodopsin-2 to multiple cell types for imaging and long-range circuit mapping. J Neurosci *28*, 7025–7030. https://doi.org/10.1523/JNEUROSCI.1954-08.2008.

44. Schnütgen, F., Doerflinger, N., Calléja, C., Wendling, O., Chambon, P., and Ghyselinck, N.B. (2003). A directional strategy for monitoring Cre-mediated recombination at the cellular level in the mouse. Nat Biotechnol *21*, 562–565. https://doi.org/10.1038/nbt811.

45. Peng, H., Bria, A., Zhou, Z., Iannello, G., and Long, F. (2014). Extensible visualization and analysis for multidimensional images using Vaa3D. Nat Protoc *9*, 193–208. https://doi.org/10.1038/nprot.2014.011.

46. Perez-Cruz, C., Nolte, M.W., van Gaalen, M.M., Rustay, N.R., Termont, A., Tanghe, A., Kirchhoff, F., and Ebert, U. (2011). Reduced spine density in specific regions of CA1 pyramidal neurons in two transgenic mouse models of Alzheimer's disease. J Neurosci *31*, 3926–3934. https://doi.org/10.1523/JNEUROSCI.6142-10.2011.

47. Horton, S., Mastrolia, V., Jackson, R.E., Kemlo, S., Pereira Machado, P.M., Carbajal, M.A., Hindges, R., Fleck, R.A., Aguiar, P., Neves, G., et al. (2024). Excitatory and inhibitory synapses show a tight subcellular correlation that weakens over development. Cell Rep *43*, 114361. https://doi.org/10.1016/j.celrep.2024.114361.

48. Bannister, N.J., and Larkman, A.U. (1995). Dendritic morphology of CA1 pyramidal neurones from the rat hippocampus: I. Branching patterns. J Comp Neurol *360*, 150–160. https://doi.org/10.1002/cne.903600111.

49. Cavalieri, D., Angelova, A., Islah, A., Lopez, C., Bocchio, M., Bollmann, Y., Baude, A., and Cossart, R. (2021). CA1 pyramidal cell diversity is rooted in the time of neurogenesis. Elife *10*, e69270. https://doi.org/10.7554/eLife.69270.

50. Lamprecht, R., and LeDoux, J. (2004). Structural plasticity and memory. Nat Rev Neurosci *5*, 45–54. https://doi.org/10.1038/nrn1301.

51. Pennacchietti, F., Vascon, S., Nieus, T., Rosillo, C., Das, S., Tyagarajan, S.K., Diaspro, A., Del Bue, A., Petrini, E.M., Barberis, A., et al. (2017). Nanoscale Molecular Reorganization of the Inhibitory Postsynaptic Density Is a Determinant of GABAergic Synaptic Potentiation. J Neurosci *37*, 1747–1756. https://doi.org/10.1523/JNEUROSCI.0514-16.2016.

52. Losonczy, A., Makara, J.K., and Magee, J.C. (2008). Compartmentalized dendritic plasticity and input feature storage in neurons. Nature *452*, 436–441. https://doi.org/10.1038/nature06725.

1149 53. Lai, C.S.W., Adler, A., and Gan, W.-B. (2018). Fear extinction reverses dendritic spine
1150 formation induced by fear conditioning in the mouse auditory cortex. Proc Natl Acad Sci
1151 U S A *115*, 9306–9311. https://doi.org/10.1073/pnas.1801504115.

1152 54. Leighton, A.H., Cheyne, J.E., and Lohmann, C. (2024). Clustered synapses develop in
1153 distinct dendritic domains in visual cortex before eye opening. Elife *12*, RP93498.
1154 https://doi.org/10.7554/eLife.93498.

1155 55. Hedrick, N.G., Wright, W.J., and Komiyama, T. (2024). Local and global predictors of
1156 synapse elimination during motor learning. Sci Adv *10*, eadk0540.
1157 https://doi.org/10.1126/sciadv.adk0540.

1158 56. Wright, W.J., Hedrick, N.G., and Komiyama, T. (2025). Distinct synaptic plasticity rules
1159 operate across dendritic compartments in vivo during learning. Science *388*, 322–328.
1160 https://doi.org/10.1126/science.ads4706.

1161 57. Nusser, Z., Lujan, R., Laube, G., Roberts, J.D., Molnar, E., and Somogyi, P. (1998).
1162 Cell type and pathway dependence of synaptic AMPA receptor number and variability
1163 in the hippocampus. Neuron *21*, 545–559. https://doi.org/10.1016/s0896-
1164 6273(00)80565-6.

1165 58. Yuste, R., and Bonhoeffer, T. (2001). Morphological changes in dendritic spines
1166 associated with long-term synaptic plasticity. Annu Rev Neurosci *24*, 1071–1089.
1167 https://doi.org/10.1146/annurev.neuro.24.1.1071.

1168 59. Bourne, J.N., and Harris, K.M. (2008). Balancing structure and function at hippocampal
1169 dendritic spines. Annu Rev Neurosci *31*, 47–67.
1170 https://doi.org/10.1146/annurev.neuro.31.060407.125646.

1171 60. Harvey, C.D., and Svoboda, K. (2007). Locally dynamic synaptic learning rules in
1172 pyramidal neuron dendrites. Nature *450*, 1195–1200.
1173 https://doi.org/10.1038/nature06416.

1174 61. Larkum, M.E. (2022). Are Dendrites Conceptually Useful? Neuroscience *489*, 4–14.
1175 https://doi.org/10.1016/j.neuroscience.2022.03.008.

1176 62. Yadav, A., Gao, Y.Z., Rodriguez, A., Dickstein, D.L., Wearne, S.L., Luebke, J.I., Hof,
1177 P.R., and Weaver, C.M. (2012). Morphologic evidence for spatially clustered spines in
1178 apical dendrites of monkey neocortical pyramidal cells. J Comp Neurol *520*, 2888–
1179 2902. https://doi.org/10.1002/cne.23070.

1180 63. Engert, F., and Bonhoeffer, T. (1997). Synapse specificity of long-term potentiation
1181 breaks down at short distances. Nature *388*, 279–284. https://doi.org/10.1038/40870.

1182 64. Schuman, E.M., and Madison, D.V. (1994). Locally distributed synaptic potentiation in
1183 the hippocampus. Science *263*, 532–536. https://doi.org/10.1126/science.8290963.

1184 65. Kastellakis, G., Tasciotti, S., Pandi, I., and Poirazi, P. (2023). The dendritic engram.
1185 Front Behav Neurosci *17*, 1212139. https://doi.org/10.3389/fnbeh.2023.1212139.

1186 66. Fu, M., Yu, X., Lu, J., and Zuo, Y. (2012). Repetitive motor learning induces
1187 coordinated formation of clustered dendritic spines in vivo. Nature *483*, 92–95.
1188 https://doi.org/10.1038/nature10844.

67. Hines, M.L., and Carnevale, N.T. (1997). The NEURON simulation environment. Neural Comput *9*, 1179–1209. https://doi.org/10.1162/neco.1997.9.6.1179.

68. Magee, J.C. (1998). Dendritic hyperpolarization-activated currents modify the integrative properties of hippocampal CA1 pyramidal neurons. J Neurosci *18*, 7613–7624. https://doi.org/10.1523/JNEUROSCI.18-19-07613.1998.

69. Golding, N.L., Mickus, T.J., Katz, Y., Kath, W.L., and Spruston, N. (2005). Factors mediating powerful voltage attenuation along CA1 pyramidal neuron dendrites. J Physiol *568*, 69–82. https://doi.org/10.1113/jphysiol.2005.086793.

70. Makarov, R., Chavlis, S., and Poirazi, P. (2024). DendroTweaks: An interactive approach for unraveling dendritic dynamics. eLife *13*. https://doi.org/10.7554/eLife.103324.1.

71. Magee, J.C., and Cook, E.P. (2000). Somatic EPSP amplitude is independent of synapse location in hippocampal pyramidal neurons. Nat Neurosci *3*, 895–903. https://doi.org/10.1038/78800.

72. Häusser, M. (2001). Synaptic function: dendritic democracy. Curr Biol *11*, R10-12. https://doi.org/10.1016/s0960-9822(00)00034-8.

73. Nicholson, D.A., Trana, R., Katz, Y., Kath, W.L., Spruston, N., and Geinisman, Y. (2006). Distance-dependent differences in synapse number and AMPA receptor expression in hippocampal CA1 pyramidal neurons. Neuron *50*, 431–442. https://doi.org/10.1016/j.neuron.2006.03.022.

74. Asrican, B., Lisman, J., and Otmakhov, N. (2007). Synaptic strength of individual spines correlates with bound Ca2+-calmodulin-dependent kinase II. J Neurosci *27*, 14007–14011. https://doi.org/10.1523/JNEUROSCI.3587-07.2007.

75. Klausberger, T., and Somogyi, P. (2008). Neuronal diversity and temporal dynamics: the unity of hippocampal circuit operations. Science *321*, 53–57. https://doi.org/10.1126/science.1149381.

76. Bezaire, M.J., Raikov, I., Burk, K., Vyas, D., and Soltesz, I. (2016). Interneuronal mechanisms of hippocampal theta oscillations in a full-scale model of the rodent CA1 circuit. Elife *5*, e18566. https://doi.org/10.7554/eLife.18566.

77. Dudok, B., Klein, P.M., Hwaun, E., Lee, B.R., Yao, Z., Fong, O., Bowler, J.C., Terada, S., Sparks, F.T., Szabo, G.G., et al. (2021). Alternating sources of perisomatic inhibition during behavior. Neuron *109*, 997-1012.e9. https://doi.org/10.1016/j.neuron.2021.01.003.

78. Price, C.J., Scott, R., Rusakov, D.A., and Capogna, M. (2008). GABA(B) receptor modulation of feedforward inhibition through hippocampal neurogliaform cells. J Neurosci *28*, 6974–6982. https://doi.org/10.1523/JNEUROSCI.4673-07.2008.

79. Szabadics, J., Tamás, G., and Soltesz, I. (2007). Different transmitter transients underlie presynaptic cell type specificity of GABAA,slow and GABAA,fast. Proc Natl Acad Sci U S A *104*, 14831–14836. https://doi.org/10.1073/pnas.0707204104.

80. Maccaferri, G., Roberts, J.D., Szucs, P., Cottingham, C.A., and Somogyi, P. (2000). Cell surface domain specific postsynaptic currents evoked by identified GABAergic

neurones in rat hippocampus in vitro. J Physiol *524 Pt 1*, 91–116. https://doi.org/10.1111/j.1469-7793.2000.t01-3-00091.x.

81. Lee, S.-H., Marchionni, I., Bezaire, M., Varga, C., Danielson, N., Lovett-Barron, M., Losonczy, A., and Soltesz, I. (2014). Parvalbumin-positive basket cells differentiate among hippocampal pyramidal cells. Neuron *82*, 1129–1144. https://doi.org/10.1016/j.neuron.2014.03.034.

82. Fuentealba, P., Begum, R., Capogna, M., Jinno, S., Márton, L.F., Csicsvari, J., Thomson, A., Somogyi, P., and Klausberger, T. (2008). Ivy cells: a population of nitric-oxide-producing, slow-spiking GABAergic neurons and their involvement in hippocampal network activity. Neuron *57*, 917–929. https://doi.org/10.1016/j.neuron.2008.01.034.

83. Skaggs, W., McNaughton, B., and Gothard, K. (1992). An Information-Theoretic Approach to Deciphering the Hippocampal Code. In Advances in Neural Information Processing Systems (Morgan-Kaufmann).

84. Mizuseki, K., Royer, S., Diba, K., and Buzsáki, G. (2012). Activity dynamics and behavioral correlates of CA3 and CA1 hippocampal pyramidal neurons. Hippocampus *22*, 1659–1680. https://doi.org/10.1002/hipo.22002.

85. Jarsky, T., Roxin, A., Kath, W.L., and Spruston, N. (2005). Conditional dendritic spike propagation following distal synaptic activation of hippocampal CA1 pyramidal neurons. Nat Neurosci *8*, 1667–1676. https://doi.org/10.1038/nn1599.

86. Bittner, K.C., Grienberger, C., Vaidya, S.P., Milstein, A.D., Macklin, J.J., Suh, J., Tonegawa, S., and Magee, J.C. (2015). Conjunctive input processing drives feature selectivity in hippocampal CA1 neurons. Nat Neurosci *18*, 1133–1142. https://doi.org/10.1038/nn.4062.

87. Stuart, G.J., and Spruston, N. (2015). Dendritic integration: 60 years of progress. Nat Neurosci *18*, 1713–1721. https://doi.org/10.1038/nn.4157.

88. Lundberg, S.M., Erion, G., Chen, H., DeGrave, A., Prutkin, J.M., Nair, B., Katz, R., Himmelfarb, J., Bansal, N., and Lee, S.-I. (2020). From Local Explanations to Global Understanding with Explainable AI for Trees. Nat Mach Intell *2*, 56–67. https://doi.org/10.1038/s42256-019-0138-9.

89. Wei, D.S., Mei, Y.A., Bagal, A., Kao, J.P., Thompson, S.M., and Tang, C.M. (2001). Compartmentalized and binary behavior of terminal dendrites in hippocampal pyramidal neurons. Science *293*, 2272–2275. https://doi.org/10.1126/science.1061198.

90. Segev, I., and Rall, W. (1998). Excitable dendrites and spines: earlier theoretical insights elucidate recent direct observations. Trends Neurosci *21*, 453–460. https://doi.org/10.1016/s0166-2236(98)01327-7.

91. Sidiropoulou, K., and Poirazi, P. (2012). Predictive features of persistent activity emergence in regular spiking and intrinsic bursting model neurons. PLoS Comput Biol *8*, e1002489. https://doi.org/10.1371/journal.pcbi.1002489.

92. Smith, S.L., Smith, I.T., Branco, T., and Häusser, M. (2013). Dendritic spikes enhance stimulus selectivity in cortical neurons in vivo. Nature *503*, 115–120. https://doi.org/10.1038/nature12600.

93. Ujfalussy, B.B., and Makara, J.K. (2020). Impact of functional synapse clusters on neuronal response selectivity. Nat Commun *11*, 1413. https://doi.org/10.1038/s41467-020-15147-6.

94. Larkum, M.E., and Nevian, T. (2008). Synaptic clustering by dendritic signalling mechanisms. Curr Opin Neurobiol *18*, 321–331. https://doi.org/10.1016/j.conb.2008.08.013.

95. Kastellakis, G., and Poirazi, P. (2019). Synaptic Clustering and Memory Formation. Front Mol Neurosci *12*, 300. https://doi.org/10.3389/fnmol.2019.00300.

96. Chirillo, M.A., Waters, M.S., Lindsey, L.F., Bourne, J.N., and Harris, K.M. (2019). Local resources of polyribosomes and SER promote synapse enlargement and spine clustering after long-term potentiation in adult rat hippocampus. Sci Rep *9*, 3861. https://doi.org/10.1038/s41598-019-40520-x.

97. Harris, K.M. (2020). Structural LTP: from synaptogenesis to regulated synapse enlargement and clustering. Curr Opin Neurobiol *63*, 189–197. https://doi.org/10.1016/j.conb.2020.04.009.

98. Karbowski, J., and Urban, P. (2024). Cooperativity, Information Gain, and Energy Cost During Early LTP in Dendritic Spines. Neural Comput *36*, 271–311. https://doi.org/10.1162/neco_a_01632.

99. Bittner, K.C., Andrasfalvy, B.K., and Magee, J.C. (2012). Ion channel gradients in the apical tuft region of CA1 pyramidal neurons. PLoS One *7*, e46652. https://doi.org/10.1371/journal.pone.0046652.

100. O'Hare, J.K., Wang, J., Shala, M.D., Polleux, F., and Losonczy, A. (2025). Distal tuft dendrites predict properties of new hippocampal place fields. Neuron, S0896-6273(25)00249-1. https://doi.org/10.1016/j.neuron.2025.03.029.

101. Bloss, E.B., Cembrowski, M.S., Karsh, B., Colonell, J., Fetter, R.D., and Spruston, N. (2018). Single excitatory axons form clustered synapses onto CA1 pyramidal cell dendrites. Nat Neurosci *21*, 353–363. https://doi.org/10.1038/s41593-018-0084-6.

102. Milstein, A.D., Li, Y., Bittner, K.C., Grienberger, C., Soltesz, I., Magee, J.C., and Romani, S. (2021). Bidirectional synaptic plasticity rapidly modifies hippocampal representations. eLife *10*, e73046. https://doi.org/10.7554/eLife.73046.

103. Magee, J.C., and Grienberger, C. (2020). Synaptic Plasticity Forms and Functions. Annual Review of Neuroscience *43*, 95–117. https://doi.org/10.1146/annurev-neuro-090919-022842.

104. Rolotti, S.V., Blockus, H., Sparks, F.T., Priestley, J.B., and Losonczy, A. (2022). Reorganization of CA1 dendritic dynamics by hippocampal sharp-wave ripples during learning. Neuron *110*, 977-991.e4. https://doi.org/10.1016/j.neuron.2021.12.017.

105. Golding, N.L., Kath, W.L., and Spruston, N. (2001). Dichotomy of action-potential backpropagation in CA1 pyramidal neuron dendrites. J Neurophysiol *86*, 2998–3010. https://doi.org/10.1152/jn.2001.86.6.2998.

106. Zhou, W.-L., Yan, P., Wuskell, J.P., Loew, L.M., and Antic, S.D. (2008). Dynamics of action potential backpropagation in basal dendrites of prefrontal cortical pyramidal

neurons. Eur J Neurosci *27*, 923–936. https://doi.org/10.1111/j.1460-9568.2008.06075.x.

107. Meyer-Dilhet, G., and Courchet, J. (2020). In Utero Cortical Electroporation of Plasmids in the Mouse Embryo. STAR Protoc *1*, 100027. https://doi.org/10.1016/j.xpro.2020.100027.

108. Virga, D.M., Hamilton, S., Osei, B., Morgan, A., Kneis, P., Zamponi, E., Park, N.J., Hewitt, V.L., Zhang, D., Gonzalez, K.C., et al. (2024). Activity-dependent compartmentalization of dendritic mitochondria morphology through local regulation of fusion-fission balance in neurons in vivo. Nat Commun *15*, 2142. https://doi.org/10.1038/s41467-024-46463-w.

109. Preibisch, S., Saalfeld, S., and Tomancak, P. (2009). Globally optimal stitching of tiled 3D microscopic image acquisitions. Bioinformatics *25*, 1463–1465. https://doi.org/10.1093/bioinformatics/btp184.

110. Ascoli, G.A. (2006). Mobilizing the base of neuroscience data: the case of neuronal morphologies. Nat Rev Neurosci *7*, 318–324. https://doi.org/10.1038/nrn1885.

111. Harris, K.M., and Kater, S.B. (1994). Dendritic spines: cellular specializations imparting both stability and flexibility to synaptic function. Annu Rev Neurosci *17*, 341–371. https://doi.org/10.1146/annurev.ne.17.030194.002013.

112. Arellano, J.I., Benavides-Piccione, R., DeFelipe, J., and Yuste, R. (2007). Ultrastructure of Dendritic Spines: Correlation Between Synaptic and Spine Morphologies. Front Neurosci *1*, 131–143. https://doi.org/10.3389/neuro.01.1.1.010.2007.

113. Peng, H., Long, F., and Myers, G. (2011). Automatic 3D neuron tracing using all-path pruning. Bioinformatics *27*, i239-247. https://doi.org/10.1093/bioinformatics/btr237.

114. Chen, J.L., Villa, K.L., Cha, J.W., So, P.T.C., Kubota, Y., and Nedivi, E. (2012). Clustered dynamics of inhibitory synapses and dendritic spines in the adult neocortex. Neuron *74*, 361–373. https://doi.org/10.1016/j.neuron.2012.02.030.

115. Shuman, T., Aharoni, D., Cai, D.J., Lee, C.R., Chavlis, S., Page-Harley, L., Vetere, L.M., Feng, Y., Yang, C.Y., Mollinedo-Gajate, I., et al. (2020). Breakdown of spatial coding and interneuron synchronization in epileptic mice. Nat Neurosci *23*, 229–238. https://doi.org/10.1038/s41593-019-0559-0.

116. Solstad, T., Moser, E.I., and Einevoll, G.T. (2006). From grid cells to place cells: a mathematical model. Hippocampus *16*, 1026–1031. https://doi.org/10.1002/hipo.20244.

117. Krächan, E.G., Fischer, A.U., Franke, J., and Friauf, E. (2017). Synaptic reliability and temporal precision are achieved via high quantal content and effective replenishment: auditory brainstem versus hippocampus. J Physiol *595*, 839–864. https://doi.org/10.1113/JP272799.

118. Bezaire, M.J., and Soltesz, I. (2013). Quantitative assessment of CA1 local circuits: knowledge base for interneuron-pyramidal cell connectivity. Hippocampus *23*, 751–785. https://doi.org/10.1002/hipo.22141.

119. Papadopoulos, P.M., Katz, M.J., and Bruno, G. (2001). NPACI: rocks: tools and techniques for easily deploying manageable Linux clusters. In Proceedings 2001 IEEE

International Conference on Cluster Computing, pp. 258–267. https://doi.org/10.1109/CLUSTR.2001.959986.

120. Hines, M.L., and Carnevale, N.T. (2001). NEURON: a tool for neuroscientists. Neuroscientist *7*, 123–135. https://doi.org/10.1177/107385840100700207.

Supplementary figures

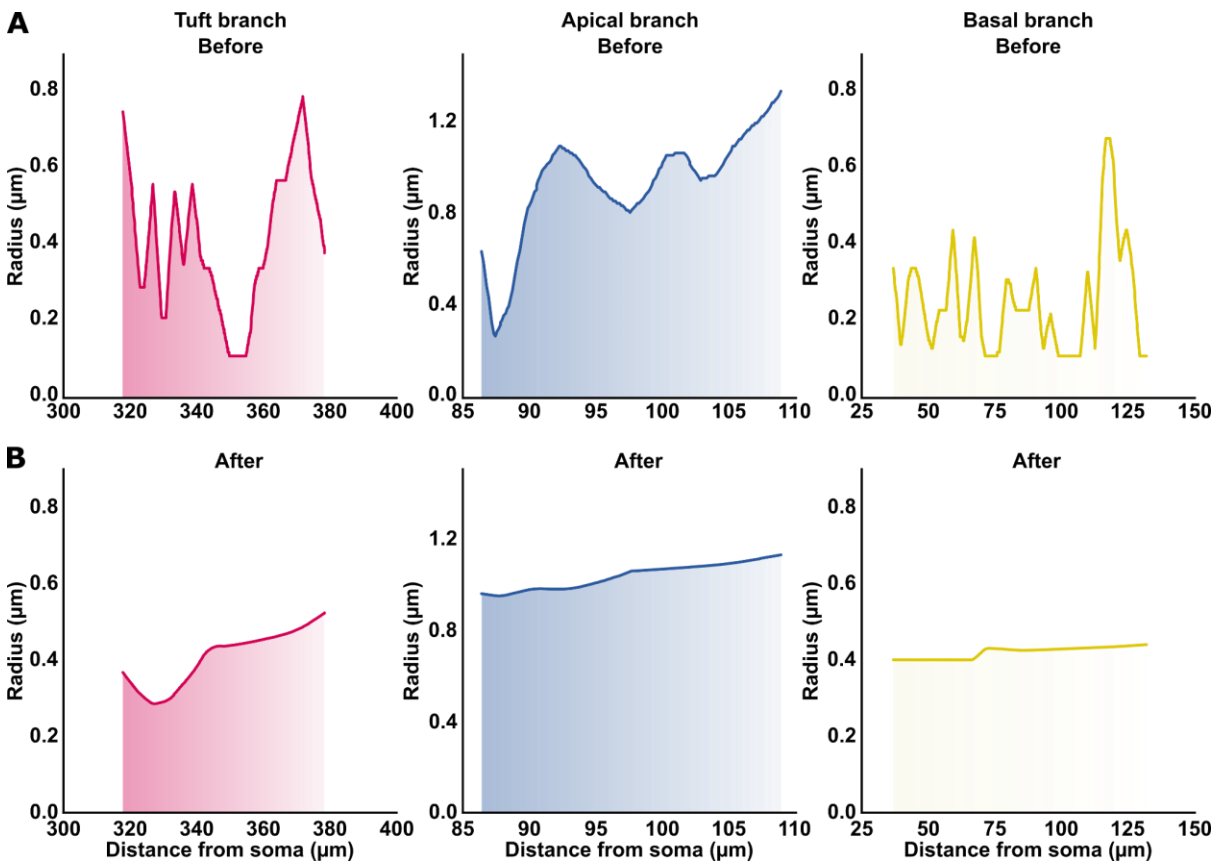

Figure S1: Dendritic diameter smoothing. *Radius profiles of three example dendritic branches before (A) and after (B) application of the smoothing algorithm. Profiles are shown for Tuft (left), Apical (center), and Basal (right) branches, with radius plotted as a function of the distance from the soma.*

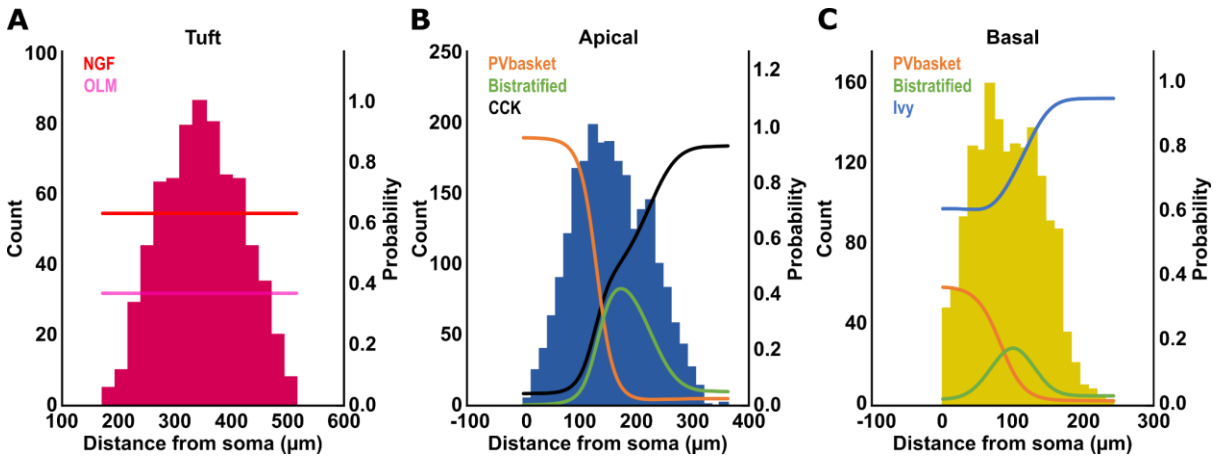

Figure S2: Probability of inhibitory input sources targeting synapses in CA1 pyramidal cells. *Distribution of inhibitory presynaptic input probabilities for synapses located on the Tuft (A), Apical (B), and Basal (C) dendrites. The probability varies with dendro-somatic path distance, capturing how different interneuron types preferentially target specific dendritic regions. Histograms show the number of synapses as a function of distance from the soma, while the overlaid curves represent the probability that a synapse is targeted by each interneuron type.*

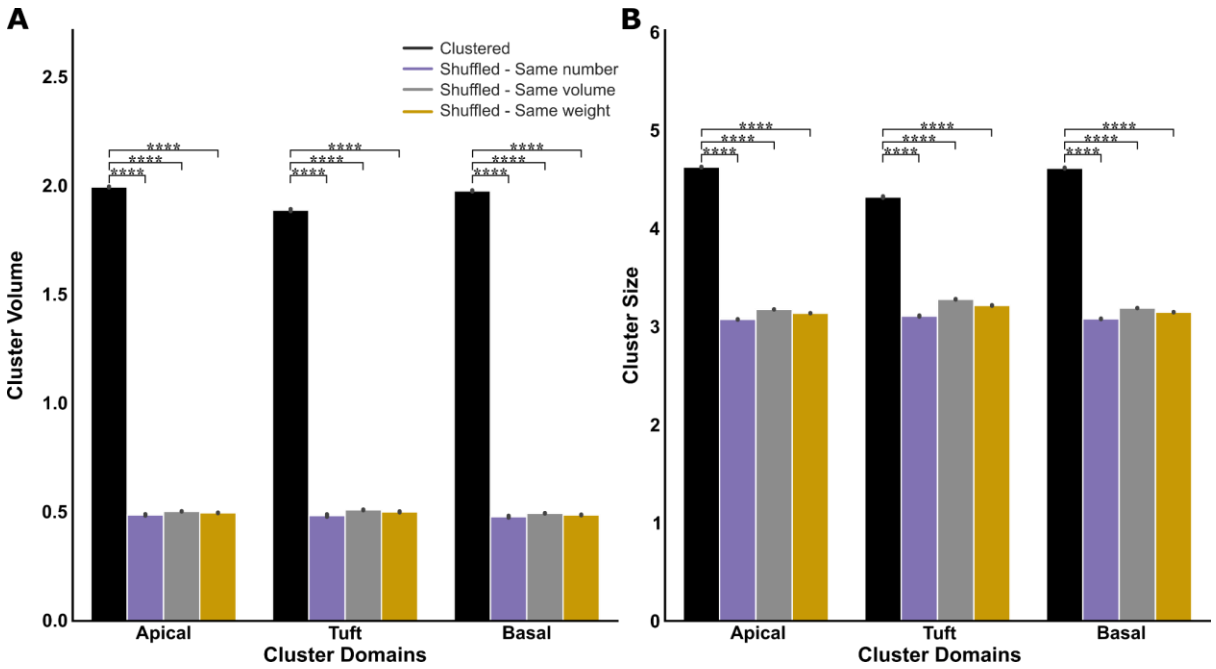

Figure S3: Characterization of synaptic clusters under alternative input allocation protocols. *Cluster volume (A) and size (B) were significantly reduced following synaptic shuffling across all protocols. Statistically significant differences were observed between the control configuration and each of the shuffled conditions, with variation maintained across dendritic domains. Pairwise t-tests between control and shuffled protocols are indicated in the plots (*p < 0.05, **p < 0.005, ***p < 0.001, and ****p < 0.0001), with corrections for multiple comparisons. Error-bars represent the 95% confidence interval (CI) of the mean.*

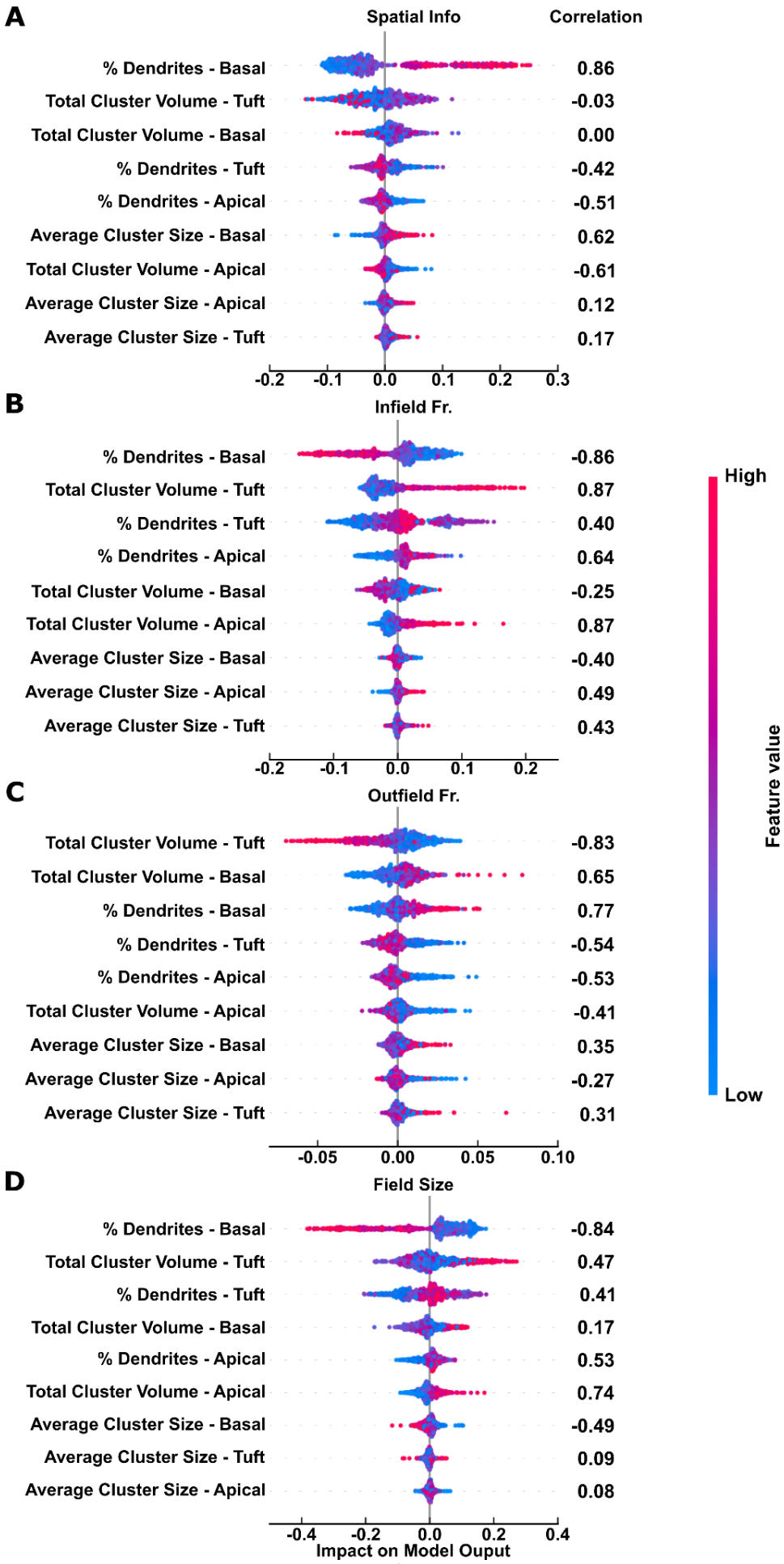
A
Spatial Info
Correlation
% Dendrites - Basal
Total Cluster Volume - Tuft
Total Cluster Volume - Basal
% Dendrites - Tuft
% Dendrites - Apical
Average Cluster Size - Basal
Total Cluster Volume - Apical
Average Cluster Size - Apical
Average Cluster Size - Tuft
0.86
-0.03
0.00
-0.42
-0.51
0.62
-0.61
0.12
0.17
-0.2 -0.1 0.0 0.1 0.2 0.3
B
Infield Fr.
% Dendrites - Basal
Total Cluster Volume - Tuft
% Dendrites - Tuft
% Dendrites - Apical
Total Cluster Volume - Basal
Total Cluster Volume - Apical
Average Cluster Size - Basal
Average Cluster Size - Apical
Average Cluster Size - Tuft
-0.86
0.87
0.40
0.64
-0.25
0.87
-0.40
0.49
0.43
-0.2 -0.1 0.0 0.1 0.2
C
Outfield Fr.
Total Cluster Volume - Tuft
Total Cluster Volume - Basal
% Dendrites - Basal
% Dendrites - Tuft
% Dendrites - Apical
Total Cluster Volume - Apical
Average Cluster Size - Basal
Average Cluster Size - Apical
Average Cluster Size - Tuft
-0.83
0.65
0.77
-0.54
-0.53
-0.41
0.35
-0.27
0.31
-0.05 0.00 0.05 0.10
D
Field Size
% Dendrites - Basal
Total Cluster Volume - Tuft
% Dendrites - Tuft
Total Cluster Volume - Basal
% Dendrites - Apical
Total Cluster Volume - Apical
Average Cluster Size - Basal
Average Cluster Size - Tuft
Average Cluster Size - Apical
-0.84
0.47
0.41
0.17
0.53
0.74
-0.49
0.09
0.08
-0.4 -0.2 0.0 0.2 0.4
Impact on Model Ouput
High
Feature value
Low

1383

Figure S4. SHAP summary plots for feature impact on spatial coding metrics. *SHAP value distributions for the prediction of four output features: (A) spatial information (bits/s), (B) in-field firing frequency (Hz), (C) out-of-field firing frequency (Hz), and (D) place field size (cm). Each dot represents a SHAP value for a given sample, with its color indicating the relative value of the corresponding input feature (blue = low, red = high). Features are ranked by their mean absolute SHAP value, reflecting their overall contribution to model output (Feature Importance). The numerical values on the right of each feature represent the Pearson correlation between the input feature values and their associated SHAP values, providing an estimate of the direction and linearity of the feature's effect on each output metric.*

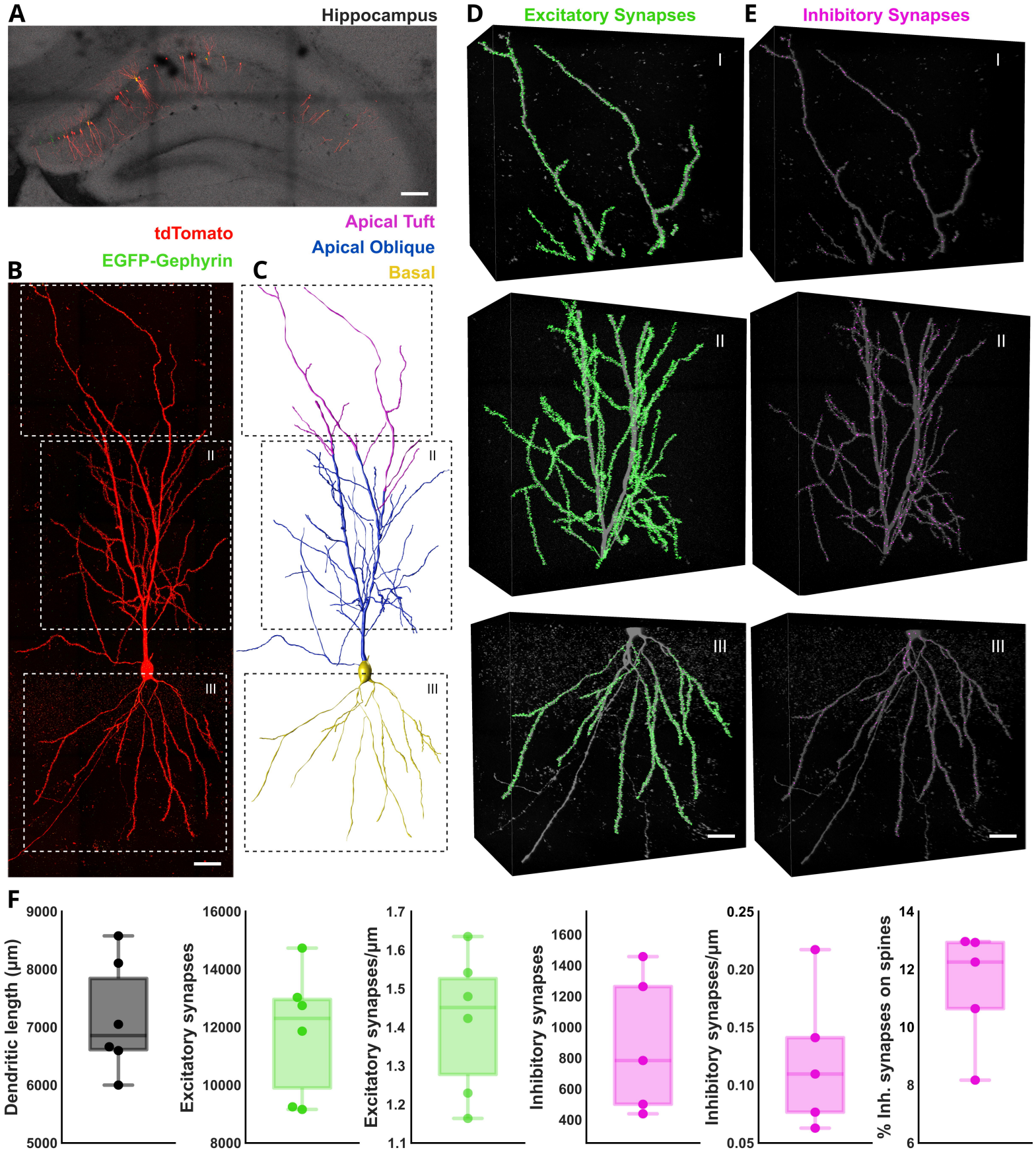
A
Hippocampus
B
tdTomato
EGFP-Gephyrin
C
Apical Tuft
Apical Oblique
Basal
D
Excitatory Synapses
E
Inhibitory Synapses
I
II
III
F
Dendritic length (µm)
9000
8000
7000
6000
5000
Excitatory synapses
16000
14000
12000
10000
8000
Excitatory synapses/µm
1.7
1.6
1.5
1.4
1.3
1.2
1.1
Inhibitory synapses
1600
1400
1200
1000
800
600
400
Inhibitory synapses/µm
0.25
0.20
0.15
0.10
0.05
% Inh. synapses on spines
14
12
10
8
6